

Optical Properties and Dielectric Functions of Grain Boundaries and Interfaces in CdTe Thin-Film Solar Cells

Budhika G Mendis, Quentin M. Ramasse, Thomas Shalvey, Jonathan D. Major, and Ken Durose

ACS Appl. Energy Mater., **Just Accepted Manuscript** • DOI: 10.1021/acsaem.8b01995 • Publication Date (Web): 22 Jan 2019

Downloaded from <http://pubs.acs.org> on January 24, 2019

Just Accepted

“Just Accepted” manuscripts have been peer-reviewed and accepted for publication. They are posted online prior to technical editing, formatting for publication and author proofing. The American Chemical Society provides “Just Accepted” as a service to the research community to expedite the dissemination of scientific material as soon as possible after acceptance. “Just Accepted” manuscripts appear in full in PDF format accompanied by an HTML abstract. “Just Accepted” manuscripts have been fully peer reviewed, but should not be considered the official version of record. They are citable by the Digital Object Identifier (DOI®). “Just Accepted” is an optional service offered to authors. Therefore, the “Just Accepted” Web site may not include all articles that will be published in the journal. After a manuscript is technically edited and formatted, it will be removed from the “Just Accepted” Web site and published as an ASAP article. Note that technical editing may introduce minor changes to the manuscript text and/or graphics which could affect content, and all legal disclaimers and ethical guidelines that apply to the journal pertain. ACS cannot be held responsible for errors or consequences arising from the use of information contained in these “Just Accepted” manuscripts.



Optical Properties and Dielectric Functions of Grain Boundaries and Interfaces in CdTe Thin-Film Solar Cells

Budhika G Mendis^{1*}, Quentin M Ramasse^{2,3}, Thomas P Shalvey⁴, Jonathan D Major⁴ and Ken Durose⁴

1. Dept of Physics, Durham University, Durham, DH1 3LE, UK

2. SuperSTEM, SciTech Daresbury Campus, Daresbury, WA4 4AD, UK

3. School of Chemical and Process Engineering, University of Leeds, Leeds, LS2 9JT, UK

4. Stephenson Institute for Renewable Energy, Dept of Physics, University of Liverpool, Liverpool, L69 7ZF, UK

*Corresponding author (b.g.mendis@durham.ac.uk)

Abstract

CdTe thin-film solar cells have complex microstructures, such as grain boundaries within the absorber layer, as well as CdS window, and Au back contact interfaces, where the local structure and chemistry undergo significant changes. The optical properties at these nano-scale defects are unknown, but their accurate measurement is required in order to identify potential losses in device efficiency. Here monochromated electron energy loss spectroscopy (EELS) in an aberration corrected scanning transmission electron microscope (STEM) is used to measure the complex dielectric function for the CdTe_{1-x}S_x inter-diffusion layer at the CdS-CdTe interface, high angle CdTe grain boundaries and Au-CdTe interface. CdTe_{1-x}S_x is shown to have a lower absorption coefficient than CdTe, but its refractive index is more closely matched to CdS. Grain boundaries have a negligible effect on the light absorption profile within CdTe, despite significant changes in the local structure and chemistry (i.e. Te-depletion) at the grain boundary. Delocalisation in inelastic scattering is the dominant systematic error in the above measurements. Finally a light backscattering mechanism via surface plasmon polaritons at the Au-CdTe interface is uncovered, which could potentially increase the photocurrent extracted from incident light at energies just above the CdTe band gap.

Keywords: dielectric function, grain boundary, inter-diffusion, CdS thin-film solar cell, monochromated EELS, aberration corrected STEM

Introduction

Thin-film solar cells, such as CdTe, utilise direct band gap semiconductors for efficient charge carrier generation through light absorption. The leading device materials, particularly CdTe, Cu(In,Ga)Se₂ and the hybrid perovskites, have in recent years exceeded 20% efficiency at the individual cell level¹, and are fast becoming commercially viable as alternatives to conventional silicon modules. In CdTe-based devices a recent innovation is to increase the short circuit current density (J_{sc}) by replacing the conventional CdS window layer with CdSe²⁻⁴. During device processing CdSe dissolves by inter-diffusion of Se into the CdTe absorber layer. The lower band gap of the CdTe_xSe_{1-x} alloy results in stronger absorption of the long

wavelength photons, while the simultaneous thinning of the CdSe window layer means that short wavelength photon losses are also minimised.

Sulphur from conventional CdS window layers is also known to inter-diffuse into the CdTe⁵⁻⁷ and lower the band gap. The sulphur inter-diffused region is however narrower in comparison to the selenium equivalent, since the former is less soluble in CdTe³. External quantum efficiency (EQE) measurements indicate that there are photocurrent losses in the ~500-600 nm wavelength range and photocurrent gains near the absorption edge threshold for devices where sulphur inter-mixing is prevalent⁸. Quantification of photocurrent losses therefore requires determining the optical properties of the CdTe_xS_{1-x} inter-diffusion layer in CdS-CdTe solar cells. This is however a challenging task since the sulphur diffusion profile shows a rapid decrease within only a few nanometres of the CdS-CdTe interface, followed by a broad, low sulphur concentration (i.e. few at%) tail extending ~500 nm into the CdTe⁶⁻⁷. Here monochromated electron energy loss spectroscopy (EELS) at high spatial resolution in an aberration corrected scanning transmission electron microscope (STEM) is used to probe the local optical properties of the inter-diffused layer⁹. By performing a Kramers-Kronig analysis of the EELS spectrum¹⁰⁻¹¹ the complex dielectric function, and hence optical properties, can be extracted, provided artefacts such as Cerenkov radiation¹² and delocalisation¹³ are minimised or taken into account.

The optical properties of other interfaces in a CdTe device, such as grain boundaries and gold back contact, are also examined. Much of the interest on grain boundaries thus far has been on their role in non-radiative recombination and the resulting losses in V_{oc} ¹⁴⁻¹⁶. Significant alteration of the structure and chemistry (e.g. chlorine segregation, tellurium depletion) can take place at a grain boundary and hence a local variation in the optical properties is possible, which may also have an impact on device performance. For example, an increase in the optical absorption at the grain boundary means that a higher fraction of photo-generated charge carriers are potentially lost to non-radiative recombination. This is exacerbated by the fact that CdTe grains are columnar in structure⁶, with grain boundaries extending through the film thickness. With high spatial and energy resolution EELS the role of CdTe grain boundaries on photo-carrier generation within the absorber layer can be evaluated for the first time. Furthermore, measurements for the gold back contact reveal a light backscattering mechanism via surface plasmon polaritons, which has the potential to increase the device photocurrent, especially at wavelengths close to the band gap of the absorber layer.

Results and Discussion

CdS_xTe_{1-x} inter-diffusion layer

Figure 1a shows a MAADF image of the CdS-CdTe interface with the CdS grain on the left hand side titled to the $[10\bar{1}0]$ zone-axis. In this orientation only the $\{111\}$ lattice planes of zinc blende CdTe are resolved and these are rotated by 24° with respect to the (0002) planes in wurtzite CdS, as determined by the image Fourier transform. Furthermore, there is a ~11% lattice mismatch between the two phases, consistent with the lattice parameters reported for bulk crystals¹⁷. The mismatch strain is thought to be the origin of the white contrast at the interface in Figure 1a.

1
2
3
4
5
6
7
8
9
10
11
12
13
14
15
16
17
18
19
20
The EELS single scattering distribution for CdS, strained interfacial region and CdTe are shown superimposed in Figure 1b. The interfacial spectrum was acquired from the box region in Figure 1a, while the CdS and CdTe spectra were acquired approximately 15 nm into the respective bulk phase. The low loss EELS spectrum was Fourier-log deconvolved¹⁰ in order to extract the single scattering distribution. The CdS spectrum thus obtained had some residual intensity from Cerenkov radiation, due to its larger band gap. This was removed by least squares fitting the spectrum to a function of the form $\alpha(E-E_g)^{1/2}$, where E is the energy loss and α , E_g are constants, over an energy window (i.e. 2.8-3.6 eV) above the band gap, extrapolating smoothly to E_g and setting all values below E_g to zero. The fitted function is based on the joint density of states for a direct band gap semiconductor with band gap E_g ¹⁸. The E_g value obtained through this procedure was 2.34 eV, and is similar to the 2.41 eV band gap obtained from reflectance and transmittance measurements of micrometre thick CdS films¹⁹.

21
22
23
24
25
26
27
28
29
30
31
32
33
34
35
36
37
38
39
40
41
42
43
44
45
46
47
48
49
The strained interfacial spectrum has characteristics of both bulk CdTe and CdS. For example, the fine structure peak 'A' is not as pronounced with respect to peaks 'B' and 'C', similar to CdS (Figure 1b; these peaks are due to interband transitions from the Cd 4*d* valence states²⁰). On the other hand the band gap of the interfacial spectrum is closer to CdTe, though slightly red shifted (Figure 1b inset). It may be argued that the CdS-CdTe interface is not atomically sharp and therefore the interfacial spectrum in Figure 1b contains contributions from both phases. To test this hypothesis the interfacial spectrum was multiple linear least squares (MLLS) fitted using three reference spectra, i.e. bulk CdTe and CdS spectra from Figure 1b as well as a delocalised spectrum, $\text{Im}\{-2/(\epsilon_{\text{CdTe}}+\epsilon_{\text{CdS}})\}$, where 'Im' represent the imaginary part of a complex number, ϵ_{CdTe} is the dielectric function for CdTe, and similarly for ϵ_{CdS} . The delocalised spectrum represents the delocalised signal for an electron moving parallel to an interface between two bulk materials²¹. It is assumed that the incident electron trajectory is primarily parallel to the interface, although with interfacial roughness the incident electron can cross from one phase into another at certain depths within the specimen, and in these situations the delocalised signal will have a different mathematical form to that of a parallel trajectory²². The CdTe, CdS dielectric functions extracted from Kramers-Kronig analysis of the single scattering distributions in Figure 1b were used to calculate the delocalised spectrum. The result of the MLLS fitting procedure is shown in Figure 1c. Some prominent features of the spectrum, such as the fine structure peak 'A' at ~13 eV, are not accurately reproduced. Furthermore, the MLLS fitting coefficient for the delocalised spectrum was an unphysical negative value, while MLLS fitting carried out with only the bulk CdTe and CdS reference spectra produced a lower quality fit. This suggests that the interfacial spectrum measured at the strained layer is not governed primarily by CdS-CdTe interface roughness.

50
51
52
53
54
55
56
57
58
59
60
The S L- and Cd, Te M-edges were acquired using core loss EELS to explore any chemical origin to the interfacial low loss EELS signal, such as the sulphur diffusion reported previously for the CdS-CdTe interface⁵⁻⁷. Figure 1d shows the S to Cd (S: Cd) and Te to Cd (Te: Cd) intensity ratio profiles across the CdS-CdTe interface, extracted from the core loss EELS data, and superimposed with the simultaneously acquired MAADF signal. The intensities have been normalised for direct visual comparison. The S: Cd and Te: Cd intensity ratios vary over a distance of ~5.2 nm at the CdS-CdTe interface. This is too large to be due to beam broadening, since with the local specimen thickness measured to be ~45 nm, the geometric probe spreading

1
2
3 for a 31 mrad STEM probe is only 1.4 nm. The fact that the atomic structure of CdS and CdTe
4 are continuous right up to the interface (Figure 1a) also suggest that beam broadening and
5 interfacial roughness are not significantly affecting the shape of the intensity ratio profiles. The
6 most probable cause therefore appears to be sulphur diffusion and the formation of a $\text{CdTe}_x\text{S}_{1-x}$
7 interfacial layer. Red shifting of the interfacial spectrum band gap with respect to CdTe (Figure
8 1b inset) also supports this conclusion¹⁹. It should be noted however that the ~500 nm broad
9 sulphur concentration tail of a few atomic% S reported in reference [6] is not observed here.
10 This is attributed to differences in the measurement technique between the two studies. In
11 reference [6] the sulphur concentration was measured using STEM energy dispersive X-ray
12 (EDX) analysis with prolonged (i.e. 1 minute per data point) counting times, while in this study
13 STEM EELS was used with an acquisition time of 0.4 s per data point. The lower peak-to-
14 background and signal-to-noise ratio for EELS under the current experimental conditions
15 makes it difficult to achieve sensitivities of a few atomic% for the S L-edge.
16
17
18
19

20 Before extracting optical properties for the $\text{CdTe}_x\text{S}_{1-x}$ interfacial layer it is necessary to discuss
21 potential artefacts in the measurement. The first is that EELS involves finite collection angles,
22 so that, strictly speaking, the results do not correspond to the ‘optical limit’, where the
23 momentum transfer $q = 0$. Nevertheless there is strong evidence to suggest that the $q = 0$
24 contribution is dominant in the EELS spectra of Figure 1b. For example, momentum resolved
25 EELS has shown that a 2 mrad scattering angle is sufficient to suppress the doublet splitting of
26 peak ‘A’ in the CdTe spectrum²⁰, although this feature is still clearly visible in Figure 1b.
27 Furthermore, the CdTe fine structure peaks are known to show very little dispersion with
28 respect to q , which is attributed to the strong interband contributions from the Cd 4*d* valence
29 electrons²⁰. Similar low loss EELS features in Figure 1b suggest that the same arguments may
30 apply to CdS and the $\text{CdTe}_x\text{S}_{1-x}$ interfacial layer as well. A second and more serious
31 measurement artefact, applicable to the $\text{CdTe}_x\text{S}_{1-x}$ layer in particular, is delocalisation in
32 inelastic scattering¹³. To evaluate its effect the EELS low loss spectrum for a 2.8 nm $\text{CdTe}_x\text{S}_{1-x}$
33 layer sandwiched between bulk CdS and CdTe was simulated using the multilayer method
34 described in reference [22-23]. The dielectric properties extracted from Kramers-Kronig
35 analysis of the EELS spectra in Figure 1b were used in the simulation. A $\text{CdTe}_x\text{S}_{1-x}$ layer
36 thickness of 2.8 nm was used since this corresponds to the Gaussian half-width of the
37 composition profiles in Figure 1d. Further details of the simulation method can be found in the
38 Supplementary Information. The simulated result is shown superimposed in Figure 1c. If
39 delocalisation were negligible the simulated spectrum should be similar to the measurement.
40 Examination of Figure 1c however shows that this is not the case; important differences are
41 apparent, particularly at energy losses corresponding to visible and near-visible light, which is
42 the operating conditions of a solar cell device. The optical properties of the $\text{CdTe}_x\text{S}_{1-x}$
43 interfacial layer reported here are therefore only approximate.
44
45
46
47
48
49

50
51 The low loss EELS spectra in Figure 1b for bulk CdTe and $\text{CdTe}_x\text{S}_{1-x}$ interfacial layer are
52 Kramers-Kronig analysed to extract the real (ϵ_1) and imaginary (ϵ_2) parts of the complex
53 dielectric function; these are shown in Figures 2a and 2b respectively. The dielectric function
54 for CdTe is qualitatively similar to that measured using spectroscopic ellipsometry²⁴. In
55 particular, the E_0 , E_1 , $E_1+\Delta_1$ and E_2 direct optical transitions are identified in the ϵ_2 plot (Figure
56 2b²⁴). The first three optical transitions are suppressed at the interfacial layer, although E_2 is
57 similar to bulk CdTe. This results in a lower absorption coefficient for the $\text{CdTe}_x\text{S}_{1-x}$ layer
58
59
60

1
2
3 compared to CdTe over the solar spectrum wavelengths that are important for a solar cell device
4 (Figure 2c). This is consistent with the results in reference [19], where apart from the
5 CdTe_{0.6}S_{0.4} composition, the absorption coefficient largely decreased on alloying CdTe with
6 sulphur. The photocurrent generated in an absorber layer depends on the absorption coefficient
7 as well as the reflectivity of light at the CdS window-absorber layer interface. A higher
8 reflectivity means that less light is transmitted into the absorber layer, and consequently the
9 photocurrent decreases. Figure 2d shows the reflectivity at normal light incidence for a CdS-
10 CdTe interface as well as CdS-CdTe_xS_{1-x}, with the CdTe_xS_{1-x} layer having the same dielectric
11 properties as that displayed in Figures 2a and 2b. The dielectric properties for CdS and CdTe
12 were extracted from the EELS spectra in Figure 1b. The reflectivity for CdS-CdTe_xS_{1-x} is an
13 improvement over the conventional CdS-CdTe interface, although the values for the latter are
14 already close to ideal.
15
16
17
18

19 The combined effects of absorption coefficient and reflectivity on the photocurrent can be
20 determined by calculating the external quantum efficiency (EQE) for devices with CdS window
21 layer and either CdTe or CdTe_xS_{1-x} absorber layer. Details of the calculation can be found in
22 the Supplementary Information, but here it should be noted that the doping concentration for
23 the two absorber layers is assumed to be identical (i.e. 10¹⁵ cm⁻³), so that the space charge width
24 in the 2.5 μm thick absorber layer is fixed at ~1.1 μm. The simulation of CdTe and CdTe_xS_{1-x}
25 absorber layers represents two extremes, since in a typical device the sulphur inter-diffused
26 region will not extend through the entire absorber layer thickness. The EQE curves for the two
27 devices are shown superimposed in Figure 2e. The spike at 480 nm is an artefact arising from
28 data processing to remove Cerenkov radiation in the CdS spectrum; it is due to the least squares
29 fitted joint density of states function and experimental curves not having exact values at the
30 point of extrapolation. There is a small increase in EQE in the plateau region for the CdTe_xS_{1-x}
31 absorber layer device; hence J_{sc} increases slightly from 18.1 to 18.3 mA/cm². The increase is
32 due to the lower reflectivity of the CdS-CdTe_xS_{1-x} interface, although its positive effects are
33 partly negated by the lower absorption coefficient. Experimentally sulphur inter-mixing gives
34 rise to a decrease in EQE in the ~500-600 nm wavelength range as well as an increased EQE
35 at the long wavelength, absorption edge threshold⁸, although this is not observed in Figure 2e.
36 This could be due to delocalisation errors in the extracted CdTe_xS_{1-x} dielectric function, and/or
37 other factors not taken into account in the EQE simulation, such as any effect of sulphur
38 alloying on carrier diffusion length and space charge width, changes in the CdS layer thickness,
39 as well as the role of CdS-absorber layer misfit strain on carrier recombination²⁵.
40
41
42
43
44
45
46

47 CdTe grain boundaries

48
49 Figure 3a is a MAADF image of a CdTe high angle grain boundary. The grain on the right has
50 been tilted to the [110] zone-axis; at this orientation the lattice planes for the left grain are not
51 resolved. Figure 3b shows the Te:Cd core loss EELS intensity ratio mapped over the box region
52 in Figure 3a. The grain boundary is Te-deficient, consistent with previous reports²⁶⁻²⁷. It has
53 also been reported that the Cd concentration can be constant across certain types of grain
54 boundary²⁶⁻²⁷. However, it was not possible to determine if this was also the case for the grain
55 boundary in Figure 3a, since strong differences in diffraction/channeling contrast between the
56 two grains meant that the Cd core loss EELS signal could not be interpreted unambiguously on
57 an absolute scale. The Te:Cd intensity ratio profile across the grain boundary was extracted
58
59
60

1
2
3 from an area close to the box region in Figure 3b and is plotted in Figure 3c. The Te:Cd intensity
4 ratio decreases by $\sim 9\%$ over a 7.4 nm region across the grain boundary. Any chlorine
5 segregation to the grain boundary from the chlorine activation process^{5,26-27} was below the
6 detection limit of core loss EELS.
7
8

9
10 The Fourier-log deconvolved EELS single scattering distribution for bulk CdTe and grain
11 boundary are shown superimposed in Figure 4a. The bulk CdTe spectrum was averaged from
12 spectra extracted from within the left and right hand grains 20 nm away from the grain
13 boundary (the two spectra were however nearly identical). The grain boundary spectrum was
14 extracted from the box region in Figure 3b. Inelastic delocalisation is again an important
15 artefact. This is evident from the simulated spectrum²²⁻²³, also shown in Figure 4a, for a 4 nm
16 grain boundary 'layer' sandwiched between two bulk CdTe grains. The dielectric constants
17 extracted from low loss EELS measurements of bulk CdTe and grain boundary were used in
18 the simulations; a grain boundary layer thickness of 4 nm was chosen since this corresponds to
19 the full width at half maximum of the Te:Cd intensity ratio profile in Figure 3c. Due to
20 delocalisation the simulated and measured grain boundary spectra do not exactly agree for the
21 energy loss range (≤ 4 eV) important for solar cell device operation. However, delocalisation
22 is not significant for the doublet 'A' peak at ~ 13 eV, and this shows a decrease at the grain
23 boundary compared to grain interior (Figure 4a).
24
25
26
27

28 Figures 4b and 4c show the real and imaginary parts of the complex dielectric function
29 extracted from Kramers-Kronig analysis of the bulk CdTe and grain boundary EELS spectra
30 in Figure 4a. The E_1 , $E_1 + \Delta_1$ and E_2 direct optical transitions are slightly suppressed at the grain
31 boundary (Figure 4c). The effect this has on the optical absorption coefficient is however
32 negligible, as can be seen from Figure 4d. Ideally the absorption coefficient at the grain
33 boundary should be as small as possible, so that the incident light generates fewer charge
34 carriers that are potentially lost to non-radiative recombination. The grain boundary analysed
35 here has a large misorientation to induce significant structural as well as chemical (i.e. Te-
36 depletion) changes locally, but to within the measurement accuracy imposed by delocalisation,
37 the change in absorption coefficient over solar spectrum wavelengths is small. In fact the
38 largest change in absorption coefficient is only observed at much higher energies (~ 9 eV).
39 Results for a different high angle grain boundary, which showed no Te-depletion, is presented
40 in the Supplementary Information. This grain boundary also displayed a decrease in the doublet
41 'A' peak at ~ 13 eV with respect to bulk CdTe, although the changes to the absorption
42 coefficient over solar spectrum wavelengths was small. The trend is therefore similar to the
43 grain boundary in Figure 3a, despite the differences in Te composition at the two boundaries.
44
45
46
47
48

49 **Gold back contact**

50
51 Figure 5a is a HAADF image of the gold back contact; the Pt layer above the gold was
52 deposited as a protective layer during FIB TEM sample preparation. The Au layer is ~ 50 nm
53 thick and has noticeable surface roughness due to the underlying grain structure of the film,
54 particularly at the interface with CdTe. Figure 5b shows the low loss EELS spectrum acquired
55 from the middle of the Au back contact layer, where a peak is observed at ~ 2.7 eV. The
56 simulated EELS spectrum for bulk Au is shown in Figure 5c and was calculated in the retarded
57 regime using the optical constants listed in reference [28]. The overall shape of the simulated
58
59
60

1
2
3 spectrum is similar to the experimental result in Figure 5b, although there are subtle
4 differences, such as the 2.7 eV peak appearing at 2.5 eV, as well as higher intensity at energy
5 losses between 1-2 eV for the experimental spectrum. These differences are possibly due to the
6 fact that the measurements were performed on a Au layer sandwiched between Pt and CdTe in
7 a thin TEM sample, so that additional surface and/or interface losses may be present, but are
8 nevertheless not taken into account in the simulation. The 2.5 eV peak in Figure 5c is due to
9 interband transitions in gold²⁸.
11

12
13 The low loss EELS spectrum extracted from the Au-CdTe interface (box region in Figure 5a)
14 is also shown in Figure 5b. The 2.7 eV peak for the Au layer is now broader and is also red
15 shifted, suggesting the presence of an additional interface loss contribution at lower energy.
16 The non-retarded surface plasmon energy at the Au-CdTe boundary is determined by the zero
17 crossing of the real part of $(\epsilon_{\text{Au}} + \epsilon_{\text{CdTe}})$, while the imaginary part must be close to zero to
18 minimise plasmon damping [28]; for simplicity the finite thickness of the Au layer is not taken
19 into account. In calculating $(\epsilon_{\text{Au}} + \epsilon_{\text{CdTe}})$ the dielectric constant in reference [28] for bulk Au
20 was used for ϵ_{Au} and the experimental values for CdTe from this work was used for ϵ_{CdTe} .
21 Figure 5d plots the real and imaginary parts of $(\epsilon_{\text{Au}} + \epsilon_{\text{CdTe}})$. A zero crossing is observed at 2
22 eV for the real part, and the imaginary part is also comparatively small in this energy range.
23 This suggests that the red shift and broadening of the 2.7 eV peak at the Au-CdTe interface is
24 due to surface plasmons at this boundary.
27

28
29 Radiative decay of surface plasmon polaritons (SPP) in noble metal nanoparticles has
30 previously been used to enhance the photocurrent extracted from silicon solar cells²⁹⁻³⁰. For a
31 perfectly flat Au-CdTe interface the surface plasmon is non-radiative, since its phase velocity
32 is smaller than the speed of light in CdTe³¹. However, when the interface is rough, such as in
33 a real device (Figure 5a), momentum can be transferred to the surface plasmon, thereby making
34 it radiative³²⁻³³. This means that in a solar cell device the light incident from the CdTe side can
35 generate SPPs that propagate along the Au-CdTe interface before radiatively decaying into a
36 photon that is backscattered into the CdTe. This is a potentially useful method for enhancing
37 the photocurrent from photons with energy slightly above the band gap of CdTe. In a
38 conventional device absorption of these low energy photons generate charge carriers deep
39 within the CdTe layer, so that they are prone to surface recombination from the Au back contact
40 or else recombine before diffusing to the space charge region. If the incident light can be
41 backscattered via SPPs however the charge carriers will be generated closer to the space charge
42 region, thereby increasing the photocurrent.
46

47
48 The maximum photocurrent gain achievable through the SPP backscattering mechanism is
49 calculated and the results are shown in Figure 6. It is assumed that all photons incident at the
50 Au-CdTe interface are backscattered and re-absorbed within the 2.5 μm thick CdTe layer.
51 Furthermore, it is assumed that the charge carriers thus generated are fully extracted by the
52 built-in electric field of the device. The photocurrent gain is calculated for photons above the
53 CdTe band gap (1.5 eV or 827 nm) up to the non-retarded surface plasmon energy (2 eV or
54 620 nm). This energy range takes into account the dispersion in surface plasmon energy³¹ as
55 well as those photons that can be absorbed by CdTe. As expected the largest gain in
56 photocurrent is for wavelengths close to the absorption threshold of CdTe. The total
57 photocurrent gain that can be achieved for all wavelengths through the SPP mechanism is 2.4
58
59
60

1
2
3 mA/cm². This is ~13% of the calculated J_{sc} value (i.e. 18.1 mA/cm²) and highlights the
4 potential of the method. A particular advantage of the SPP mechanism is that the metal back
5 contact is part of the solar cell device architecture, so that the efficiency can potentially be
6 increased without a radical alteration in device fabrication. The mechanism is also transferrable
7 to thin-film solar cells other than CdTe. Nevertheless questions remain on the efficiency of
8 SPP excitation by light and subsequent radiative decay, the ideal surface roughness of the Au
9 back contact and ideal thickness of CdTe absorber layer. A more in-depth analysis is required
10 to investigate these factors further.
11
12
13

14 **Conclusions**

15
16
17 Aberration corrected and monochromated STEM EELS is used to measure the local optical
18 properties of interfaces in CdTe thin-film solar cells. Delocalisation in inelastic scattering was
19 found to be a limiting factor in the accuracy of such high spatial resolution measurements. The
20 dielectric function measured for the CdTe_{1-x}S_x inter-diffusion layer at the CdS-CdTe interface
21 indicated a smaller band gap, but a lower optical absorption coefficient over much of the solar
22 spectrum range. Reflection losses of light at the CdS-CdTe_{1-x}S_x interface is however lower than
23 CdS-CdTe. The benefits of improved reflectivity on the photocurrent is therefore offset by the
24 lower absorption coefficient, resulting in only a modest change in J_{sc} . Sulphur inter-mixing has
25 previously been identified as a contributing factor to J_{sc} losses, but this effect is not observed
26 here. This could be due to systematic errors in the data arising from delocalisation artefacts, as
27 well as the unknown effects of sulphur alloying on materials parameters (i.e. carrier diffusion
28 length, doping concentration etc).
29
30
31
32

33 Subtle variations in optical transitions are also observed at CdTe grain boundaries, which are
34 due to the abrupt change in the structure and/or chemistry (e.g. Te-depletion) at the grain
35 boundary. However, this gives rise to only minor changes in the absorption coefficient in the
36 visible or near-visible spectrum range at the grain boundary compared to the grain interior.
37 Ideally the grain boundary should have a low absorption coefficient, so that any charge carriers
38 generated by light absorption are not lost to non-radiative recombination via band gap defect
39 states. However, the results here suggest that grain boundaries in CdTe do not have a significant
40 impact on the carrier generation profile within the absorber layer.
41
42
43

44 Measurements at the Au back contact-CdTe interface revealed a surface plasmon at ~2 eV. The
45 Au layer is not smooth due to the underlying grain structure, and this surface roughness can
46 cause the surface plasmon to couple with an electromagnetic field. Light incident from the
47 CdTe side can therefore excite surface plasmon polaritons (SPP) at the Au-CdTe interface,
48 which subsequently backscatter the light into the CdTe through radiative decay. If optimised
49 this has the potential to increase the photocurrent for light wavelengths close to the absorption
50 threshold of CdTe.
51
52
53

54 **Experimental Method**

55 **Device fabrication**

56
57
58
59
60

1
2
3 100 nm of CdS was radio frequency (RF) sputter deposited at 200°C under 5 mTorr of argon
4 on NSG Ltd TEC 15M glass. CdTe was subsequently close space sublimation (CSS) deposited
5 after a substrate pre-anneal at 450°C for 20 mins. The source and substrate temperatures during
6 CSS deposition were 610° and 520°C respectively. A two-stage deposition for 20 mins under
7 20 Torr of nitrogen followed by a 20 second vacuum deposition step at the same temperatures
8 was used. The thickness of the CdTe absorber layer was ~2.5 µm. Samples were then etched
9 in a nitric-phosphoric (NP) acid solution for 30 seconds³⁴ prior to a MgCl₂ activation step³⁵ for
10 30 mins at 410°C in air. This was followed by a further NP etch for 15 seconds before thermal
11 evaporation of a 50 nm thick gold back contact.
12
13
14

15 **Electron Microscopy**

16
17
18 Cross-sections of the completed devices were thinned to electron transparency using an FEI
19 Helios 600 focussed ion beam (FIB) microscope, with the final ion-beam voltage during
20 thinning being 2 kV. The sample thickness was in the range of 25-45 nm, as determined by
21 Kramers-Kronig analysis of EELS spectra (see below). Samples were examined in the Nion
22 UltraSTEM 100 MC Hermes microscope at the SuperSTEM facility, Daresbury. Apart from
23 the high spatial resolution due to the aberration corrected optics of the STEM column, this
24 microscope is also capable of simultaneously achieving ~10 meV EELS energy resolution⁹,
25 although in this work a dispersion of 20 meV/channel was used to acquire the low loss EELS
26 spectra. Thus some energy resolution was sacrificed, limited by the point spread function of
27 the detector, in order to increase the energy loss range (up to 37 eV) recorded in a single EELS
28 spectrum; this is required in order to perform an accurate Kramers-Kronig analysis³⁶. Chemical
29 analysis was performed using core loss EELS with a dispersion of 0.3 eV/channel. The STEM
30 probe semi-convergence angle was 31 mrad and the EELS collection semi-angle was 44 mrad.
31 Images were simultaneously acquired using a medium angle annular dark field (MAADF)
32 detector (55, 82 mrad inner and outer angles) as well as a high angle annular dark field
33 (HAADF) detector (82, 180 mrad inner and outer angles). The operating voltage of the
34 microscope was reduced to 60 kV in order to minimise Cerenkov radiation artefacts.
35 Simulation of the electron energy loss function in the retarded and non-retarded regimes³⁷ using
36 the dielectric properties for CdTe¹⁹ showed that Cerenkov losses were negligible for the
37 experimental conditions in this work. Kramers-Kronig analysis was performed using Gatan
38 Digital Micrograph software. A combined Gaussian and Lorentzian model was used to fit the
39 zero loss peak (ZLP) in the EELS spectra.
40
41
42
43
44
45

46 **Supporting Information**

47
48 Includes (i) Multi-layer simulation of EELS spectra, (ii) External Quantum Efficiency (EQE)
49 calculation of a solar cell device and (iii) Optical properties of a CdTe grain boundary showing
50 no Te-depletion.
51
52
53

54 **Acknowledgments**

55
56 Instrument time at the EPSRC National Research Facility for Advanced Electron Microscopy,
57 SuperSTEM, is gratefully acknowledged.
58
59
60

References

- [1] Green M.A.; Hishikawa Y.; Warta W.; Dunlop E.D.; Levi D.H.; Hohl-Ebinger J.; Ho-Baillie A.W.H. Solar Cell Efficiency Tables (version 51), *Prog. Photovolt: Res. Appl.* **2018**, *26*, 3-12.
- [2] Paudel N.R.; Yan Y. Enhancing the Photo-currents of CdTe Thin-Film Solar Cells in both Short and Long Wavelength Regions, *Appl. Phys. Lett.* **2014**, *105*, 183510 (5 pages).
- [3] Poplawsky J.D.; Guo W.; Paudel N.; Ng A.; More K.; Leonard D.; Yan Y. Structural and Compositional Dependence of the CdTe_xSe_{1-x} Alloy Layer Photoactivity in CdTe-based Solar Cells, *Nature Comms.* **2016**, *7*, 12537 (9 pages).
- [4] Baines T.; Zoppi G.; Bowen L.; Shalvey T.P.; Mariotti S.; Durose K.; Major J.D. Incorporation of CdSe Layers into CdTe Thin Film Solar Cells, *Sol. Energy Mat. Sol. Cells* **2018**, *180*, 196-204.
- [5] Terheggen M.; Heinrich H.; Kostorz G.; Romeo A.; Bätzner D.; Tiwari A.N.; Bosio A.; Romeo N. Structural and Chemical Interface Characterisation of CdTe Solar Cells by Transmission Electron Microscopy, *Thin Solid Films* **2003**, *431*, 262-266.
- [6] Taylor A.A.; Major J.D.; Kartopu G.; Lamb D.; Duenow J.; Dhere R.G.; Maeder X.; Irvine S.J.C.; Durose K.; Mendis B.G. A Comparative Study of Microstructural Stability and Sulphur Diffusion in CdS/CdTe Photovoltaic Devices, *Sol. Energy Mat. Sol. Cells* **2015**, *141*, 341-349.
- [7] Poplawsky J.D.; Li C.; Paudel N.R.; Guo W.; Yan Y.; Pennycook S.J. Nanoscale Doping Profiles Within CdTe Grain Boundaries and at the CdS/CdTe Interface Revealed by Atom Probe Tomography and STEM EBIC, *Sol. Energy Mat. Sol. Cells* **2016**, *150*, 95-101.
- [8] Demtsu S.H.; Sites J.R. Quantification of Losses in Thin-Film CdS/CdTe Solar Cells, *Proceedings of the 31st IEEE Photovoltaic Specialist Conference* **2005**, pp. 347-350.
- [9] Krivanek O.L.; Ursin J.P.; Bacon N.J.; Corbin G.J.; Delby N.; Hrnčirik P.; Murfitt M.F.; Own C.S.; Szilagyí Z.S. High Energy Resolution Monochromator for Aberration Corrected Scanning Transmission Electron Microscopy/Electron Energy Loss Spectroscopy, *Phil. Trans. R. Soc. A* **2009**, *367*, 3683-3697.
- [10] Egerton R.F. *Electron Energy Loss Spectroscopy in the Electron Microscope*, Second Edition, Plenum Press, New York, **1996**.
- [11] Stöger-Pollach M. Optical Properties and Band Gaps from Low Loss EELS: Pitfalls and Solutions, *Micron* **2008**, *39*, 1092-1110.
- [12] Stöger-Pollach M.; Schattschneider P. The Influence of Relativistic Energy Losses on Bandgap Determination using Valence EELS, *Ultramicroscopy* **2007**, *107*, 1178-1185.

- 1
2
3 [13] Muller D.A.; Silcox J. Delocalisation in Inelastic Scattering, *Ultramicroscopy* **1995**, *59*,
4 195-213.
5
6
7 [14] Major J.D.; Proskuryakov Y.Y.; Durose K.; Zoppi G.; Forbes I. Control of Grain Size in
8 Sublimation-grown CdTe, and the Improvement in Performance of Devices with
9 Systematically Increased Grain Size, *Sol. Energy Mat. Sol. Cells* **2010**, *94*, 1107-1112.
10
11
12 [15] Mendis B.G.; Bowen L.; Jiang Q.Z. A Contactless Method for Measuring the
13 Recombination Velocity of an Individual Grain Boundary in Thin-Film Photovoltaics, *Appl.*
14 *Phys. Lett.* **2010**, *97*, 092112 (3 pages).
15
16
17 [16] Mendis B.G.; Gachet D.; Major J.D.; Durose K. Long Lifetime Hole Traps at Grain
18 Boundaries in CdTe Thin-Film Photovoltaics, *Phys. Rev. Lett.* **2015**, *115*, 218701 (5 pages).
19
20
21 [17] Wood D.A.; Rogers K.D.; Lane D.W.; Conibeer G.J.; Parton D. A Study of the Phase
22 Boundaries and Lattice Parameters of the CdS-CdTe Pseudobinary System, *J. Mat. Sci. Lett.*
23 **1998**, *17*, 1511-1514.
24
25
26 [18] Rafferty B.; Brown L.M. Direct and Indirect Transitions in the Region of the Band Gap
27 using Electron Energy Loss Spectroscopy, *Phys. Rev. B* **1998**, *58*, 10326-10337.
28
29
30 [19] Wood D.A.; Rogers K.D.; Lane D.W.; Coath J.A. Optical and Structural Characterisation
31 of CdS_xTe_{1-x} Thin Films for Solar Cell Applications, *J. Phys.: Condens. Matter* **2000**, *12*, 4433-
32 4450.
33
34
35 [20] Dröge H.; Fleszar A.; Hanke W.; Sing M.; Knupfer M.; Fink J.; Goschenhofer F.; Becker
36 C.R.; Kargerbauer R.; Steinrück H.P. Complex Loss Function of CdTe, *Phys. Rev. B* **1999**, *59*,
37 5544-5550.
38
39
40 [21] Wang Z.L. Valence Electron Excitations and Plasmon Oscillations in Thin Films,
41 Surfaces, Interfaces, and Small Particles, *Micron* **1996**, *27*, 265-299.
42
43
44 [22] Bolton J.P.R.; Chen M. Electron Energy Loss in Multi-Layered Slabs, *Ultramicroscopy*
45 **1995**, *60*, 247-263.
46
47
48 [23] Bolton J.P.R.; Chen M. Electron Energy Loss in Multi-Layered Slabs: I. Normal
49 Incidence, *J. Phys.: Condens. Matter* **1995**, *7*, 3373-3387.
50
51
52 [24] Adachi S.; Kimura T.; Suzuki N. Optical Properties of CdTe: Experiment and Modelling,
53 *J. Appl. Phys.* **1993**, *74*, 3435-3441.
54
55
56 [25] Mendis B.G.; Treharne R.E.; Lane D.W.; Durose K. The Effects of Junction Interdiffusion
57 and Misfit Dislocations on the Efficiency of Highly Mismatched Heterojunction Photovoltaic
58 Devices, *Appl. Phys. Lett.* **2016**, *108*, 183505 (5 pages).
59
60

1
2
3 [26] Li C.; Poplawsky J.; Wu Y.; Lupini A.R.; Mouti A.; Leonard D.N.; Paudel N.; Jones K.;
4 Yin W.; Al-Jassim M.; Yan Y.; Pennycook S.J. From Atomic Structure to Photovoltaic
5 Properties in CdTe Solar Cells, *Ultramicroscopy* **2013**, *134*, 113-125.
6
7

8 [27] Li C.; Wu Y.; Poplawsky J.; Pennycook T.J.; Paudel N.; Yin W.; Haigh S.J.; Oxley M.P.;
9 Lupini A.R.; Al-Jassim M.; Pennycook S.J.; Yan Y. Grain Boundary-Enhanced Carrier
10 Collection in CdTe Solar Cells, *Phys. Rev. Lett.* **2014**, *112*, 156103 (5 pages).
11
12

13 [28] Johnson P.B.; Christy R.W. Optical Constants of the Noble Metals, *Phys. Rev. B* **1972**, *6*,
14 4370-4379.
15
16

17 [29] Pillai S.; Catchpole K.R.; Trupke T.; Green M.A. Surface Plasmon Enhanced Silicon Solar
18 Cells, *J. Appl. Phys.* **2007**, *101*, 093105 (8 pages).
19
20

21 [30] Temple T.L.; Mahanama G.D.K.; Reehal H.S.; Bagnall D.M. Influence of Localised
22 Surface Plasmon Excitation in Silver Nanoparticles on the Performance of Silicon Solar Cells,
23 *Sol. Energy Mat. Sol. Cells* **2009**, *93*, 1978-1985.
24
25

26 [31] Pitarke J.M.; Silkin V.M.; Chulkov E.V.; Echenique P.M. Theory of Surface Plasmons
27 and Surface-Plasmon Polaritons, *Rep. Prog. Phys.* **2007**, *70*, 1-87.
28
29

30 [32] Teng Y.Y.; Stern E.A. Plasma Radiation from Metal Grating Surfaces, *Phys. Rev. Lett.*
31 **1967**, *19*, 511-514.
32
33

34 [33] Kuttge M.; Vesseur E.J.R.; Koenderink A.F.; Lezec H.J.; Atwater H.A.; Garcia de Abajo
35 F.J.; Polman A. Local Density of States, Spectrum, and Far-Field Interference of Surface
36 Plasmon Polaritons Probed by Cathodoluminescence, *Phys. Rev. B* **2009**, *79*, 113405 (4 pages).
37
38

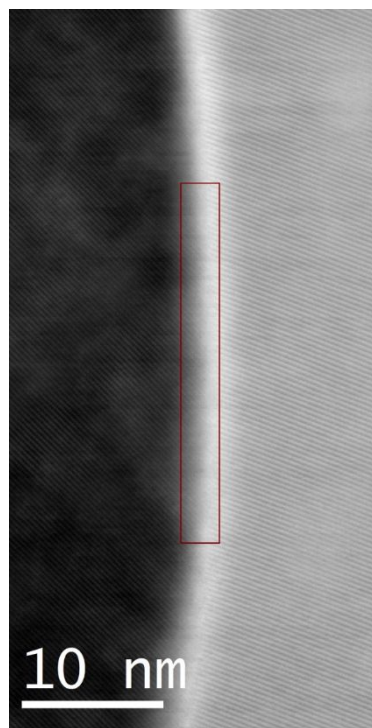
39 [34] Major J.D.; Proskuryakov Y.Y.; Durose K. Impact of CdTe Surface Composition on
40 Doping and Device Performance in Close Space Sublimation Deposited CdTe Solar Cells,
41 *Prog. Photovolt: Res. Appl.* **2013**, *21*, 436-443.
42
43

44 [35] Major J.D.; Treharne R.E.; Phillips L.J.; Durose K. A Low Cost Non-Toxic Post-Growth
45 Activation Step for CdTe Solar Cells, *Nature* **2014**, *511*, 334-337.
46
47

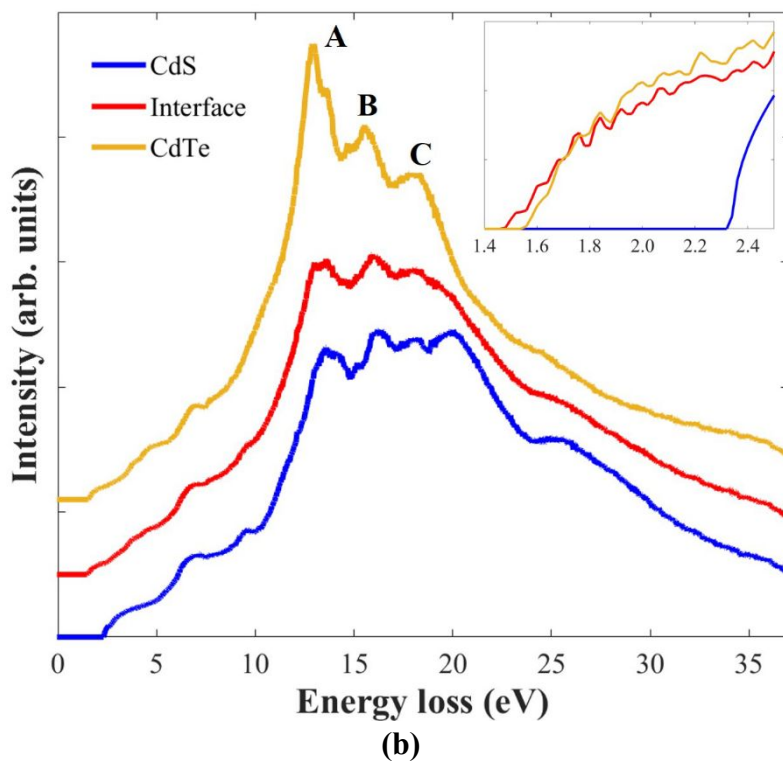
48 [36] Alexander J.A.; Scheltens F.J.; Drummy L.F.; Durstock M.F.; Hage F.S.; Ramasse Q.M.;
49 McComb D.W. High Resolution Monochromated Electron Energy Loss Spectroscopy of
50 Organic Photovoltaic Materials, *Ultramicroscopy* **2017**, *180*, 125-132.
51
52

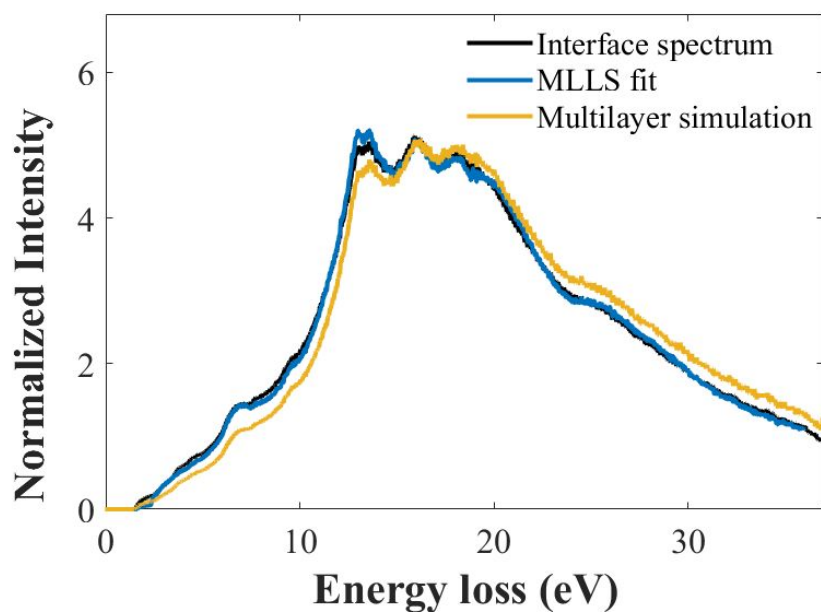
53 [37] Erni R.; Browning N.D. The Impact of Surface and Retardation Losses on Valence
54 Electron Energy Loss Spectroscopy, *Ultramicroscopy* **2008**, *108*, 84-99.
55
56
57
58
59
60

Figures

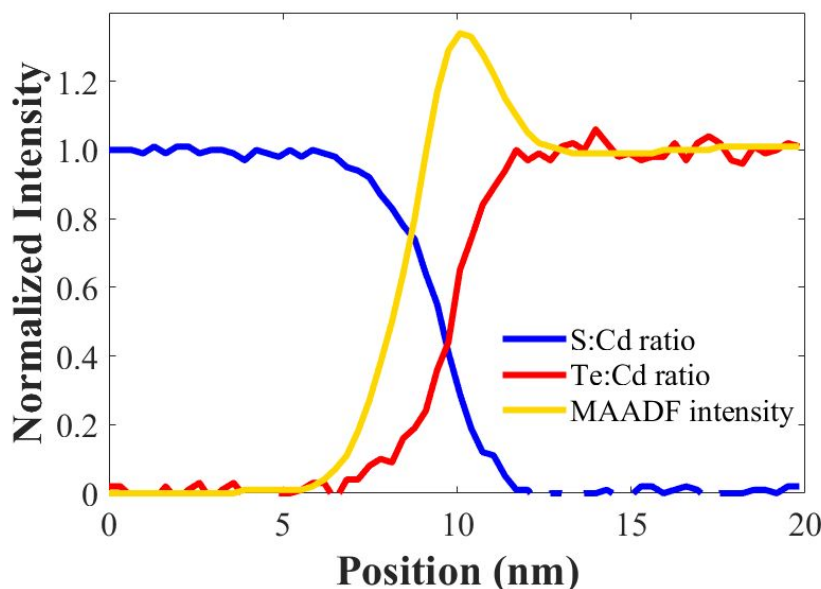


(a)



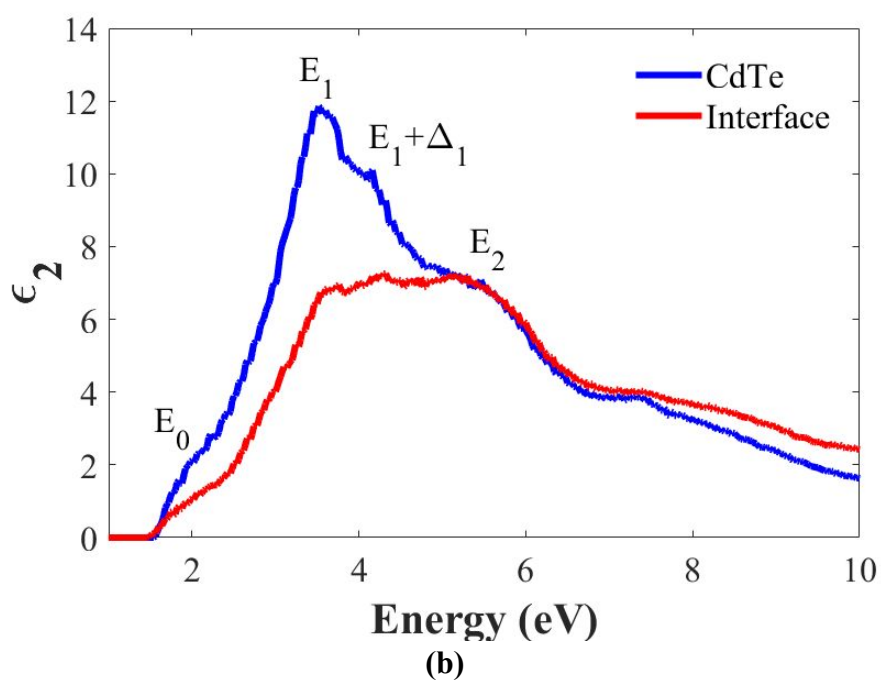
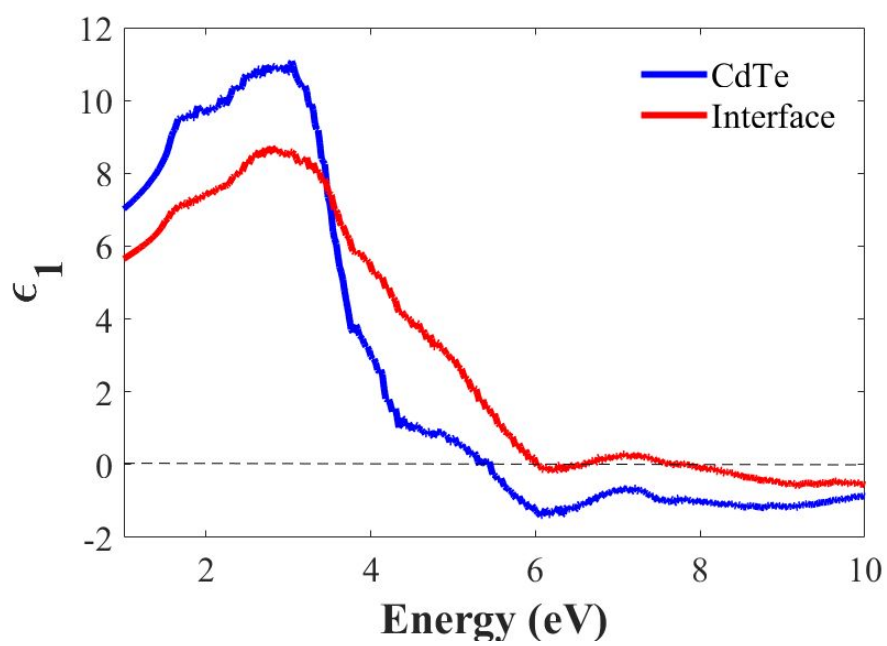


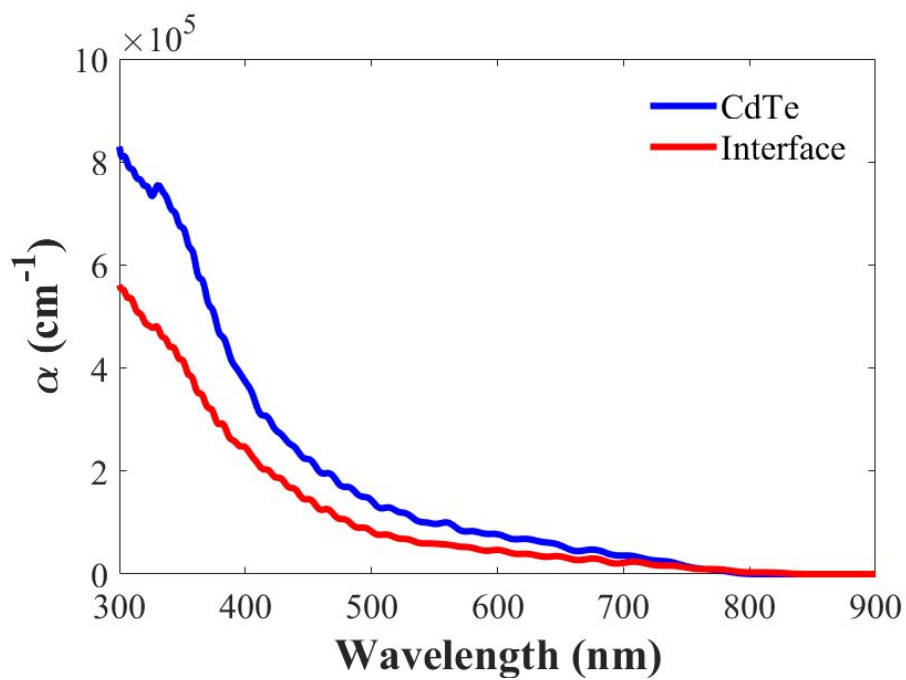
(c)



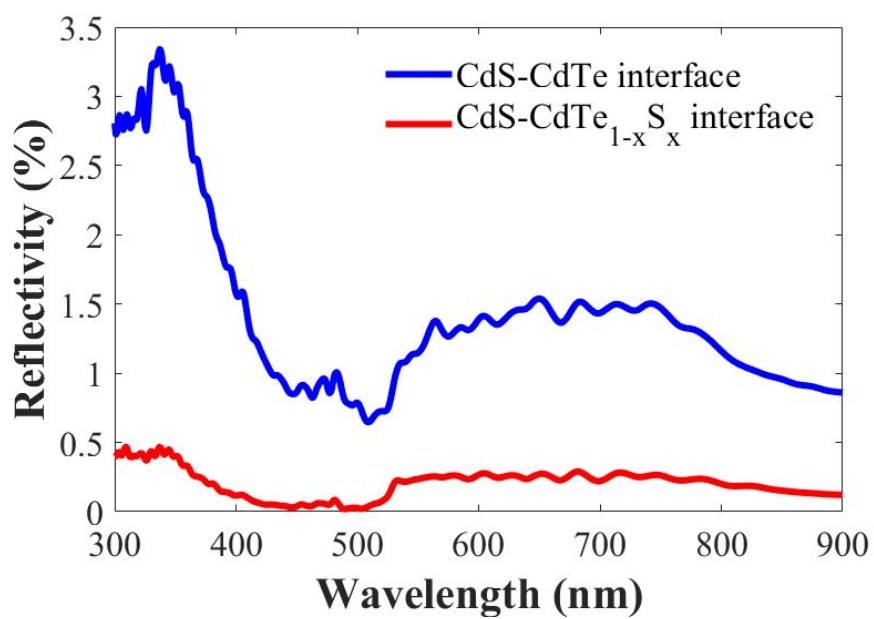
(d)

Figure 1: (a) MAADF image of the CdS-CdTe interface. (b) EELS single scattering distributions for CdS, CdTe and the CdS-CdTe interface extracted from the box region in Figure 1a. The inset shows the energy loss onset for the three spectra. (c) shows the CdS-CdTe interface spectrum and the multiple linear least squares (MLLS) fit using CdS, CdTe and a delocalised signal as the reference spectra. The delocalised signal has the form $\text{Im}\{-2/(\epsilon_{\text{CdTe}} + \epsilon_{\text{CdS}})\}$, where ϵ_{CdTe} , ϵ_{CdS} are the dielectric functions for CdS and CdTe respectively and ‘Im’ represents the imaginary part of a complex number. Also shown in Figure 1c is the simulated spectrum for a 2.8 nm $\text{CdTe}_{1-x}\text{S}_x$ layer sandwiched between bulk CdS and CdTe. Analytical expressions for a multilayer system²⁴⁻²⁵ were used in the simulation. The area under the curves in Figure 1c is normalised for direct comparison. (d) shows the S: Cd and Te: Cd core loss EELS intensity ratio profiles across the CdS-CdTe interface, along with the MAADF intensity. The curves have been normalised for direct comparison.





(c)



(d)

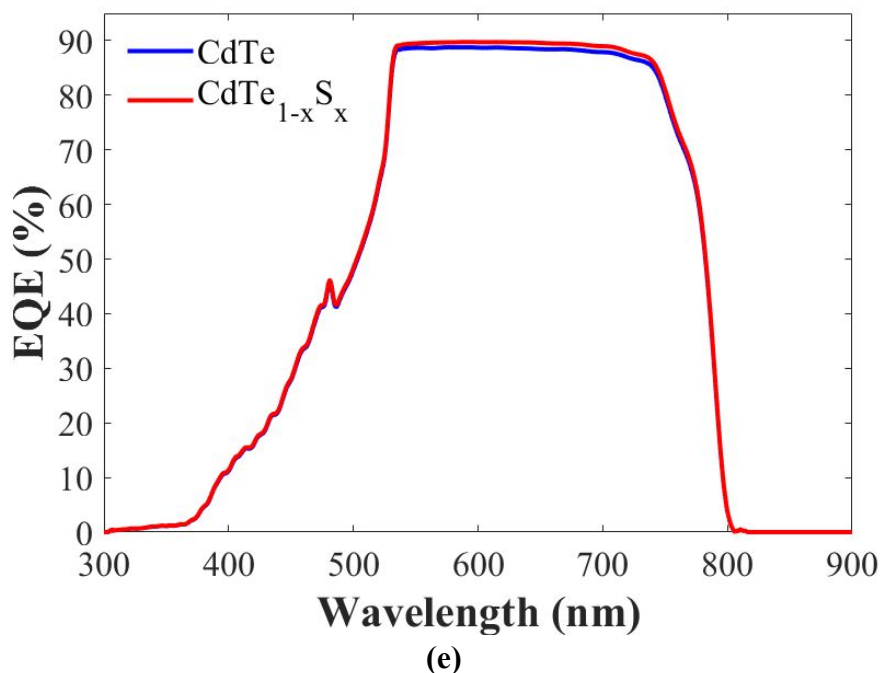
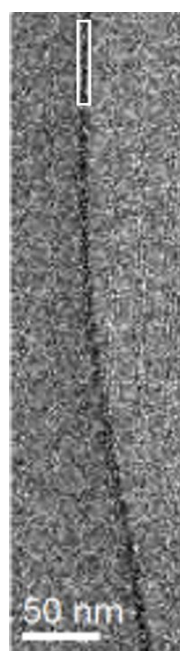
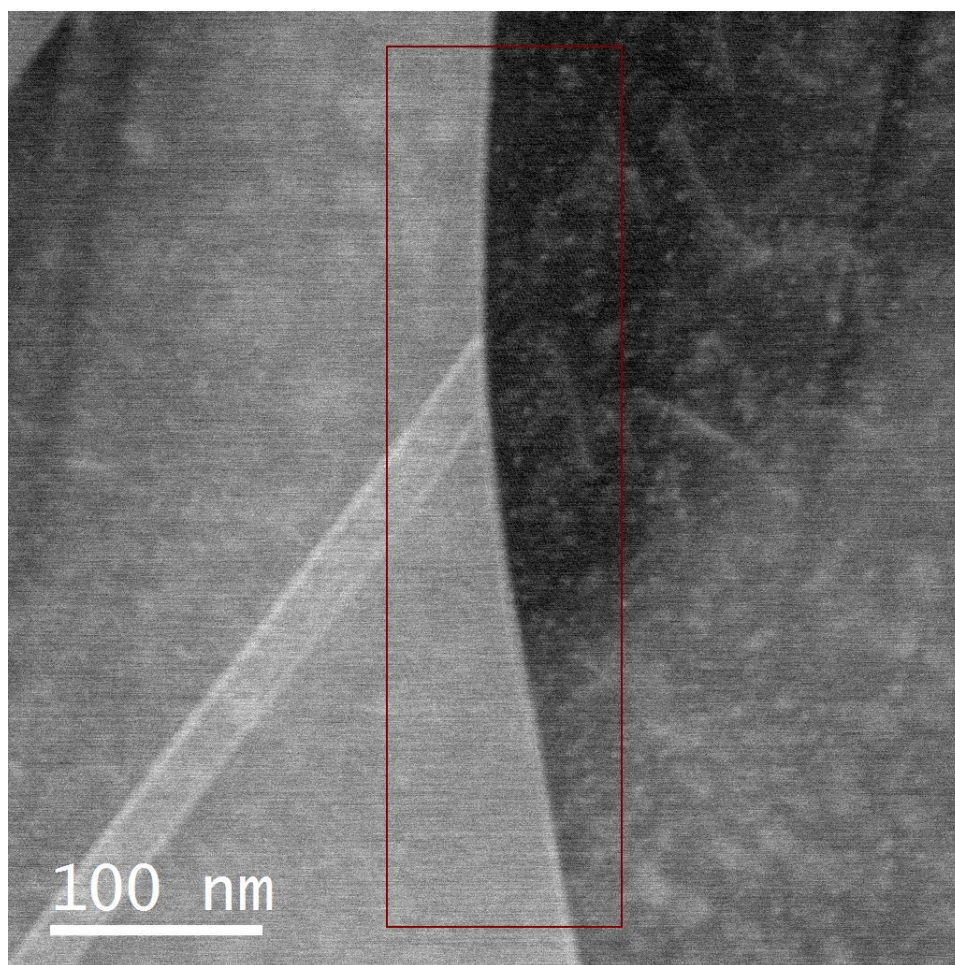


Figure 2: (a) real (ϵ_1) and (b) imaginary (ϵ_2) parts of the complex dielectric function for the CdTe_{1-x}S_x interface layer and bulk CdTe, extracted from a Kramers-Kronig analysis of the EELS spectra in Figure 1b. The absorption coefficient (α) over solar spectrum wavelengths important for solar cell device operation is plotted in (c). (d) shows the reflectivity as a function of wavelength for a CdS-CdTe interface and CdS-CdTe_{1-x}S_x interface. The simulated external quantum efficiency (EQE) for the CdS-CdTe and CdS-CdTe_{1-x}S_x devices are plotted in (e).



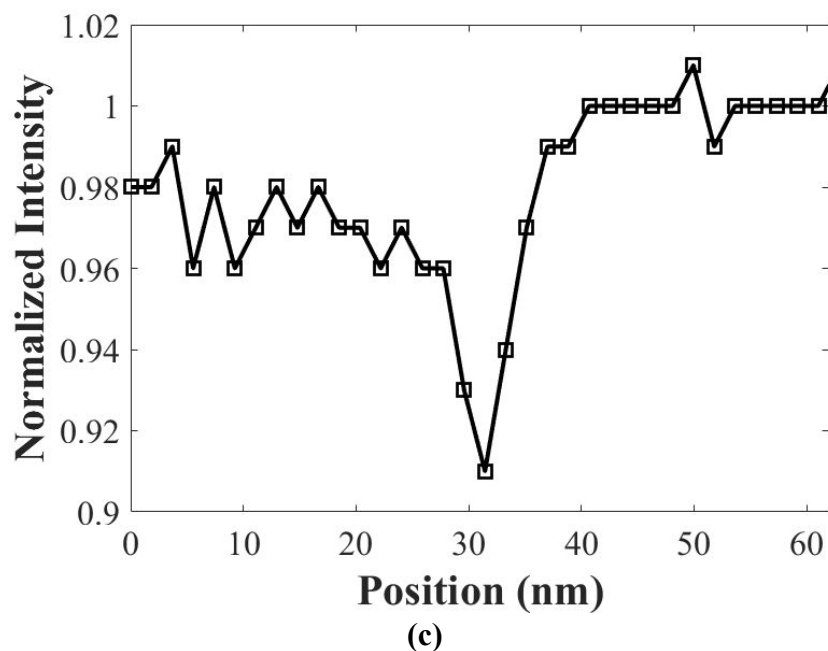
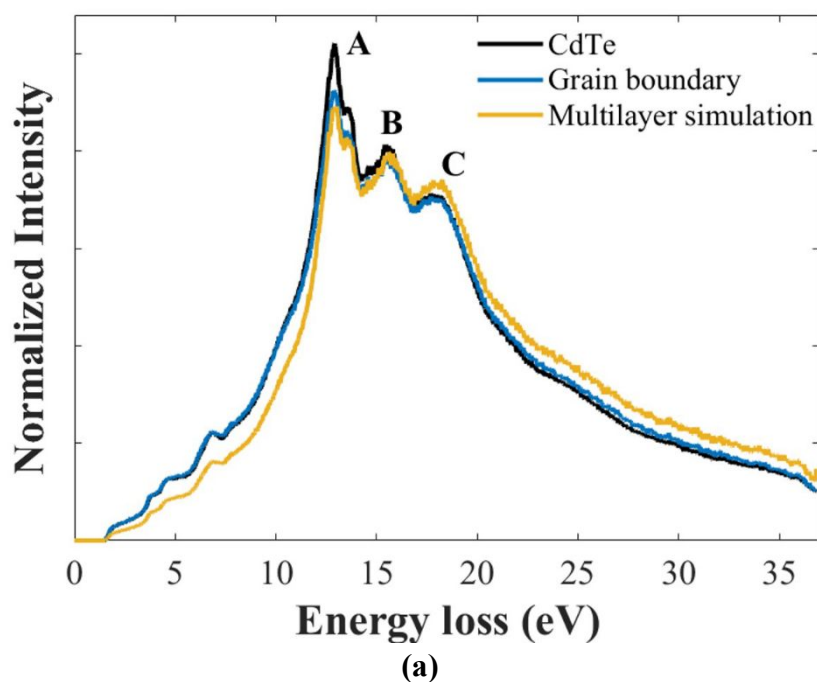
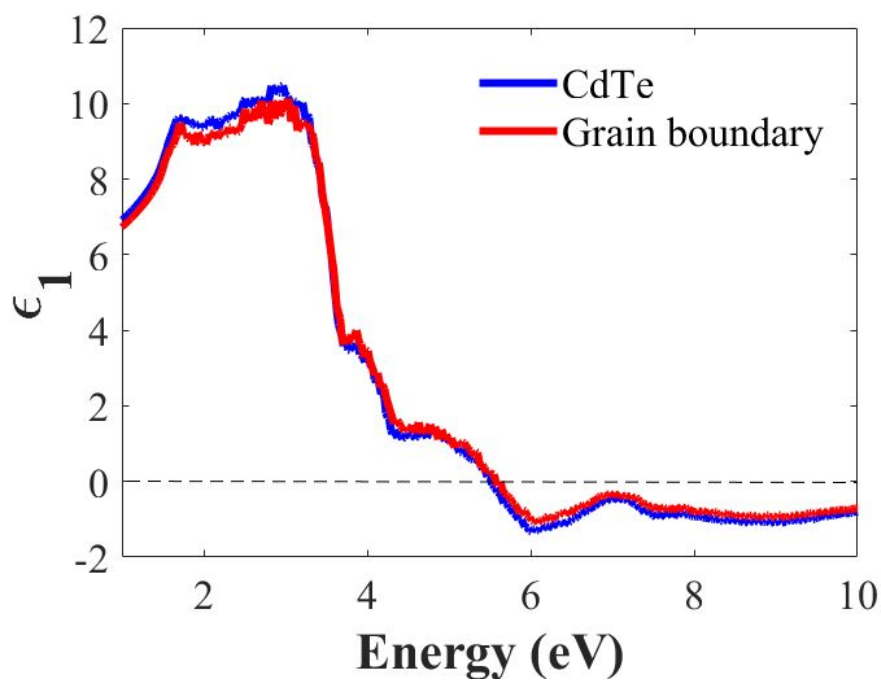
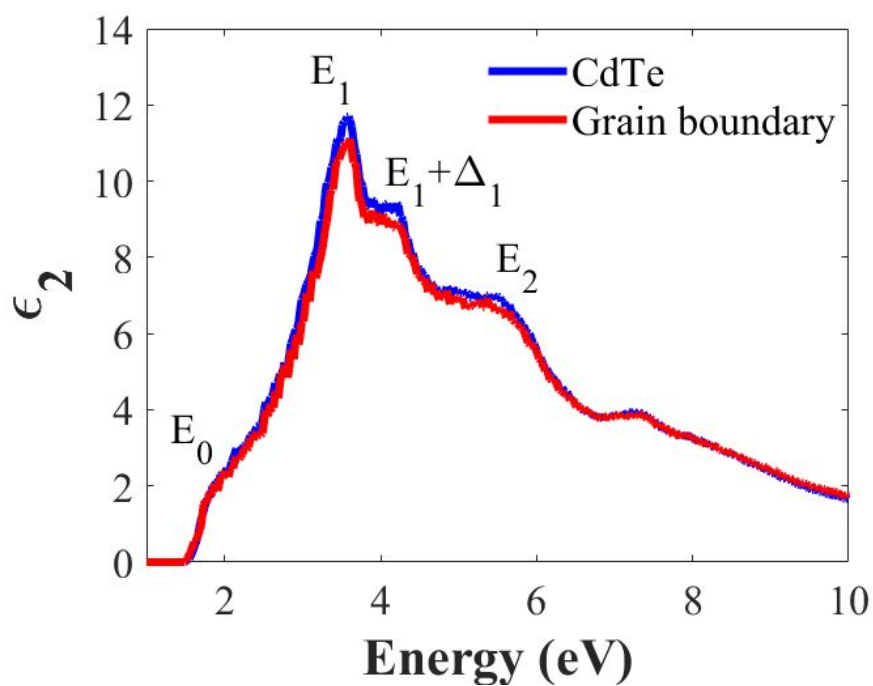


Figure 3: (a) MAADF image of a high angle CdTe grain boundary. (b) shows the Te: Cd core loss EELS intensity ratio mapped over the box region in Figure 3a. The Te: Cd intensity ratio profile across the grain boundary is shown in (c). The profile was extracted from an area close to the box region in Figure 3b. The average Te: Cd ratio for the grain interior on the right hand side has been normalised to unity.





(b)



(c)

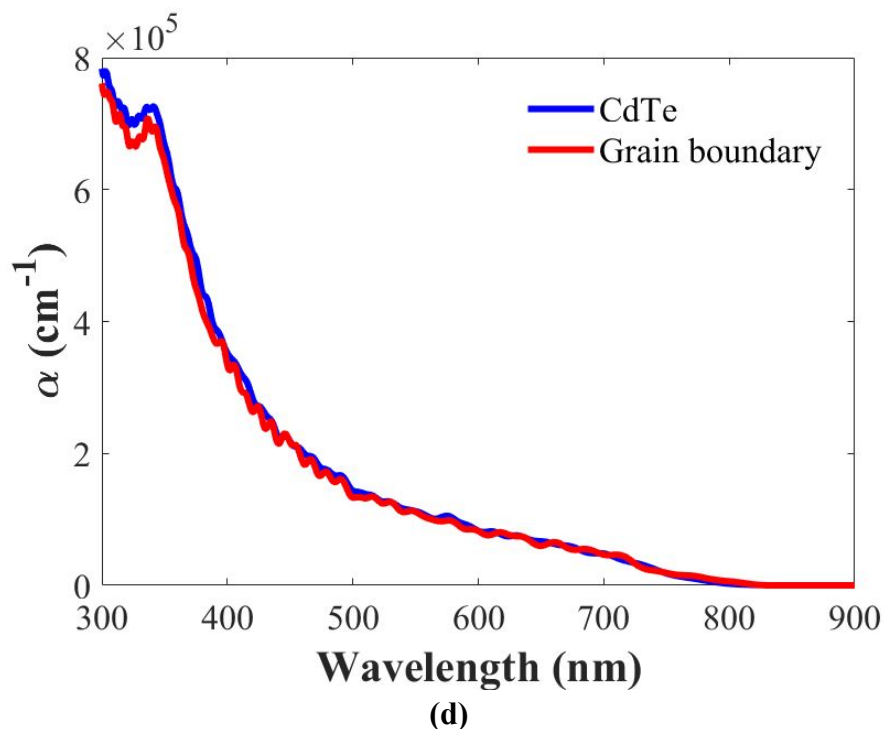
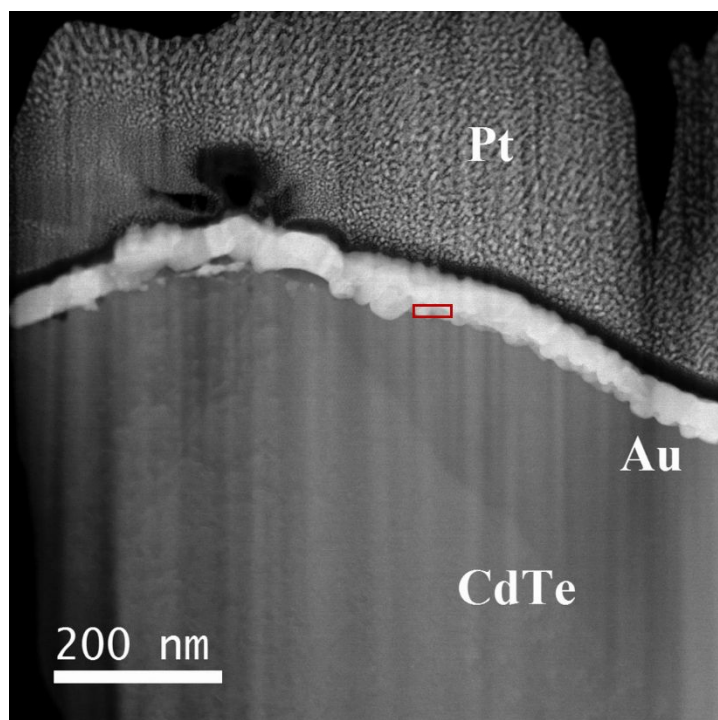
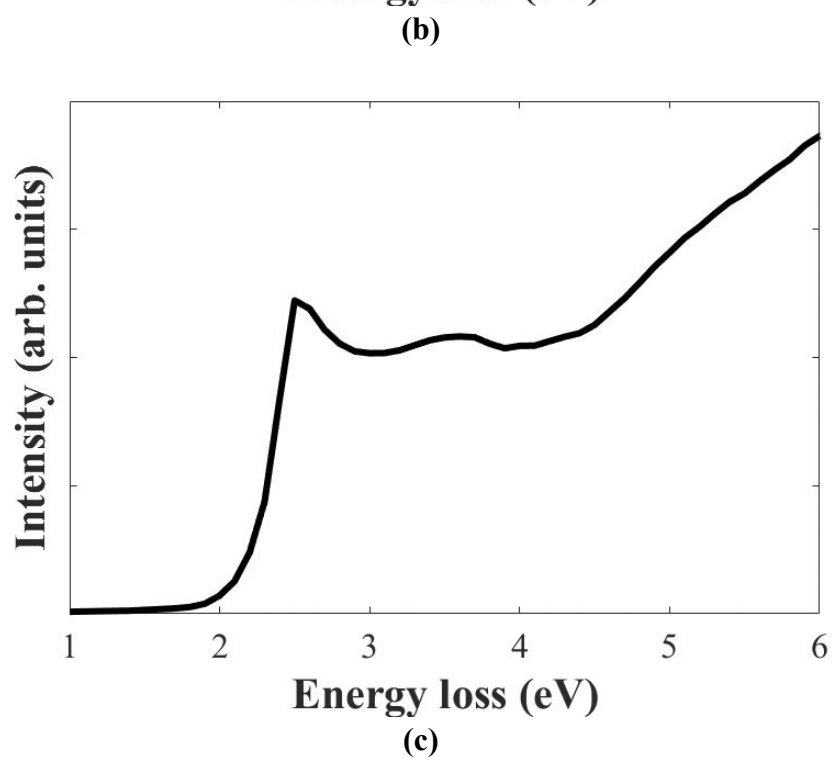
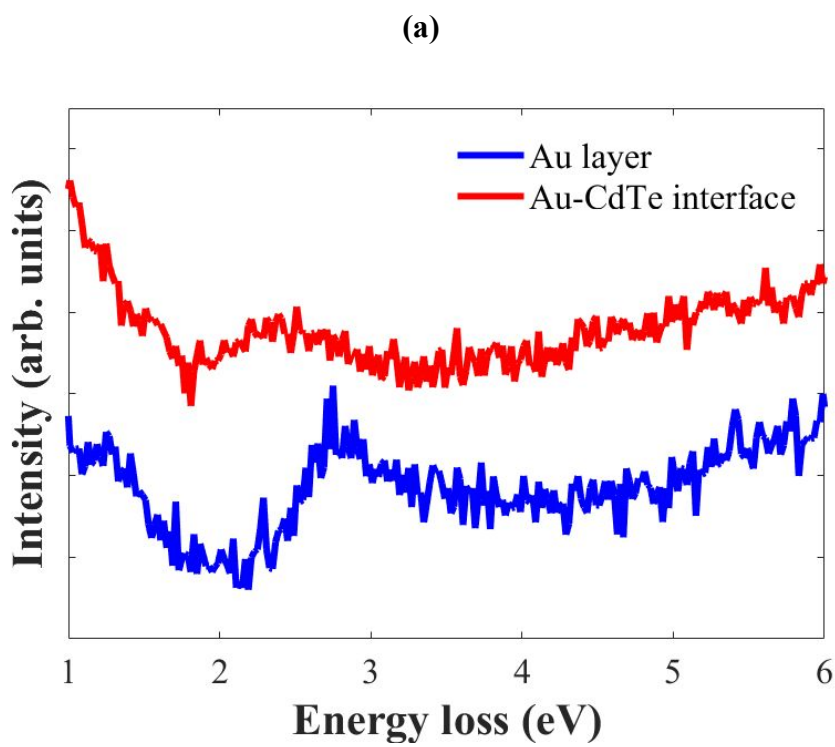


Figure 4: (a) EELS single scattering distributions for bulk CdTe and CdTe grain boundary are superimposed with the area under the curves normalised for direct comparison. The grain boundary spectrum was extracted from the box region in Figure 3b. Also shown in Figure 4a is the simulated spectrum for a 4 nm grain boundary ‘layer’ sandwiched between bulk CdTe. Analytical expressions for a multilayer system²⁴⁻²⁵ were used in the simulation. The real (ϵ_1) and imaginary (ϵ_2) parts of the complex dielectric function for CdTe and CdTe grain boundary are shown in (b) and (c) respectively. The corresponding absorption coefficient (α) over solar spectrum wavelengths for solar cell device operation is plotted in (d).





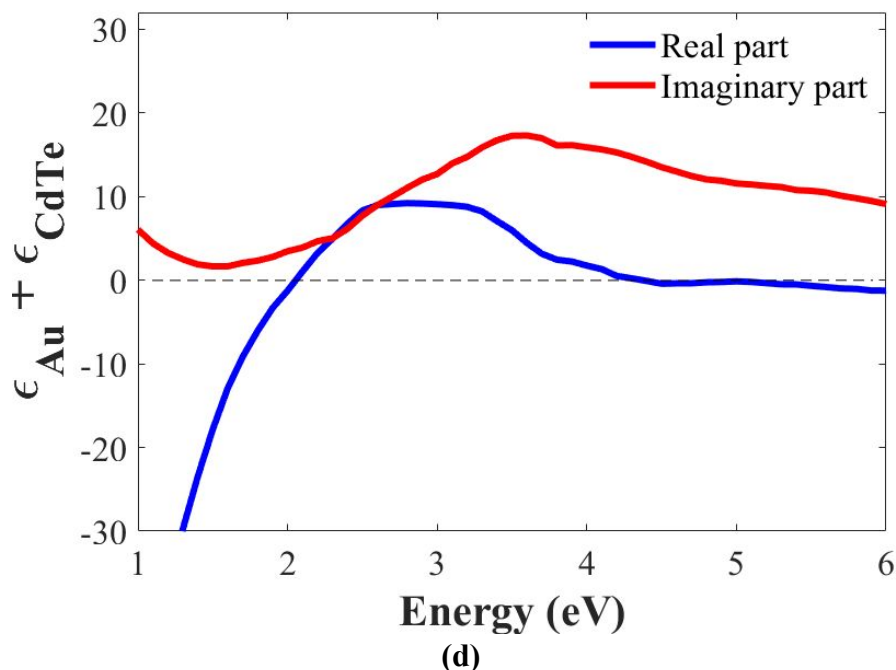


Figure 5: (a) HAADF image of Au-CdTe interface. The Pt overlayer was deposited during FIB TEM specimen preparation. (b) Low loss EELS spectra for the Au layer and Au-CdTe interface. The latter was extracted from the box region in Figure 5a. The zero loss peak has not been subtracted from the individual spectra, although its intensity was normalised for a more direct comparison. (c) shows the low loss EELS spectrum for bulk gold simulated in the retarded regime. The real and imaginary part of $(\epsilon_{\text{Au}} + \epsilon_{\text{CdTe}})$, where ϵ_{Au} , ϵ_{CdTe} are the dielectric functions for Au and CdTe respectively, is shown in (d).

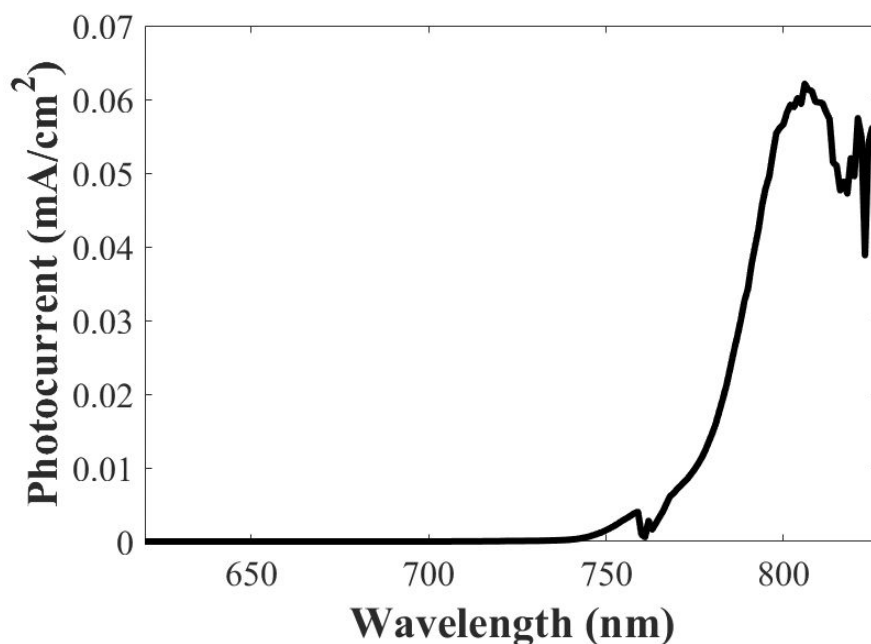
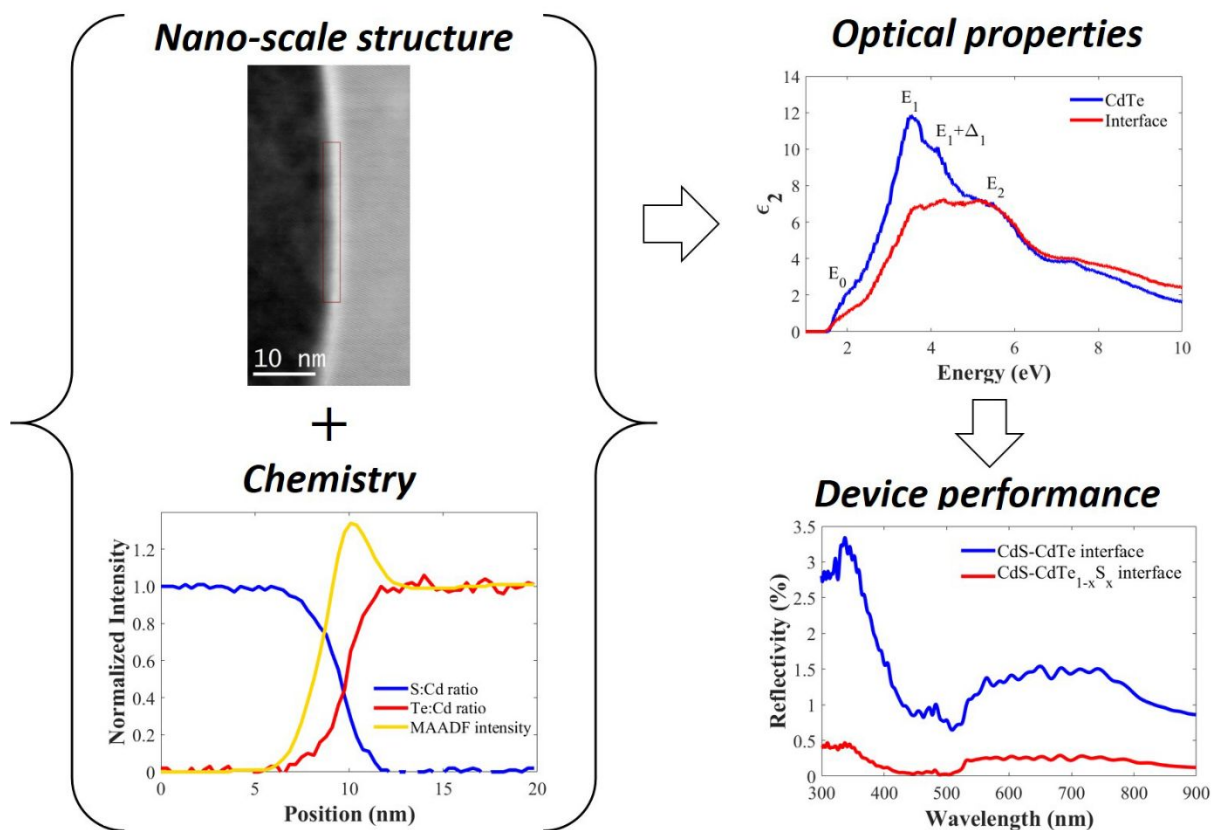


Figure 6: Photocurrent gain as a function of wavelength of incident light for the surface plasmon polariton (SPP) mechanism in a 2.5 μm thick CdTe film with Au back contact. It is

1
2
3 assumed that all the light incident on the Au layer is SPP backscattered and re-absorbed within
4 the CdTe to produce charge carriers with 100% collection efficiency.
5
6
7
8
9
10
11
12
13
14
15
16
17
18
19
20
21
22
23
24
25
26
27
28
29
30
31
32
33
34
35
36
37
38
39
40
41
42
43
44
45
46
47
48
49
50
51
52
53
54
55
56
57
58
59
60

Graphical Table of Contents



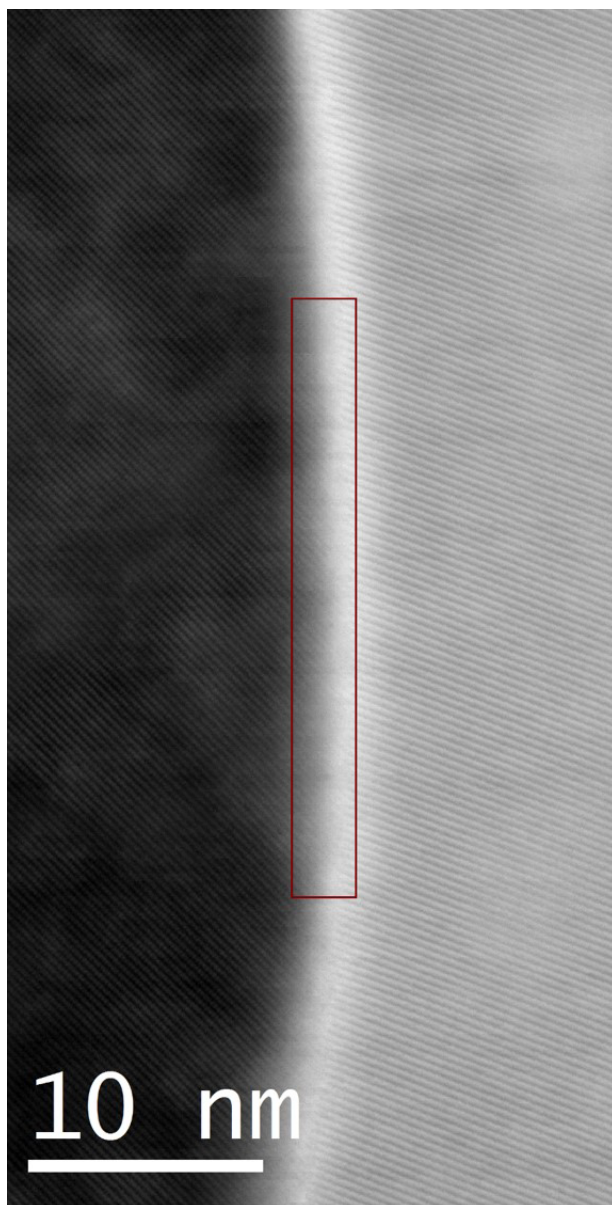


Figure 1a

97x190mm (150 x 150 DPI)

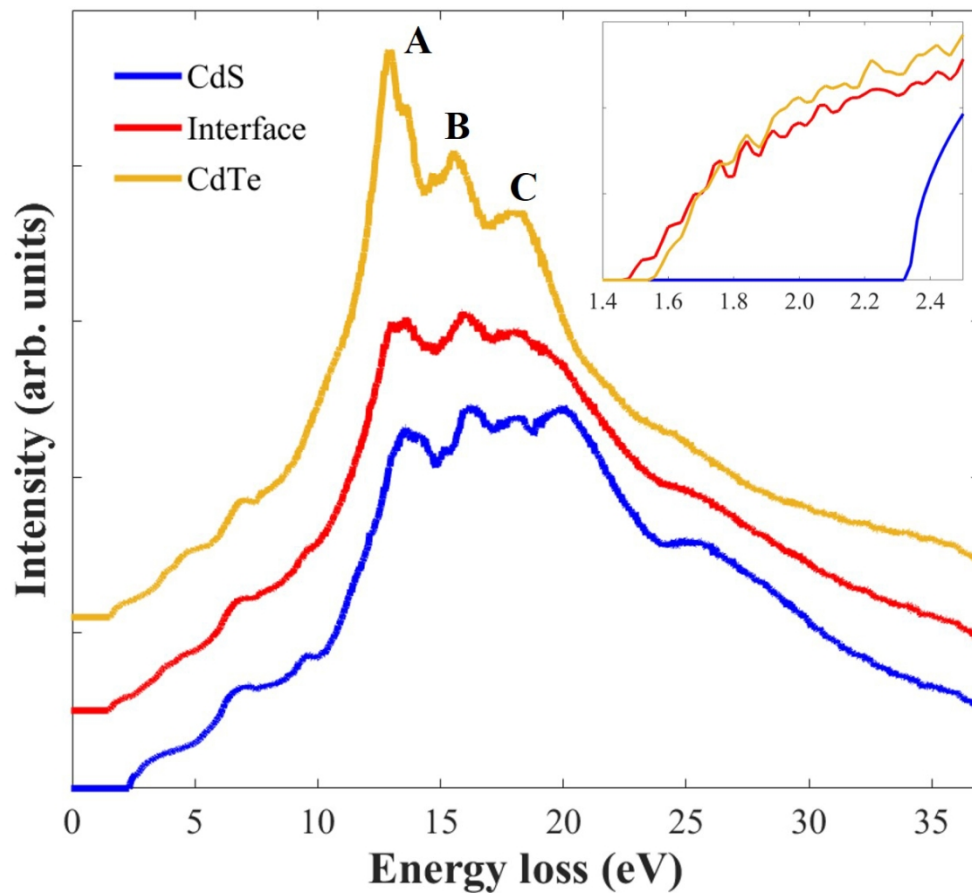


Figure 1b

213x190mm (150 x 150 DPI)

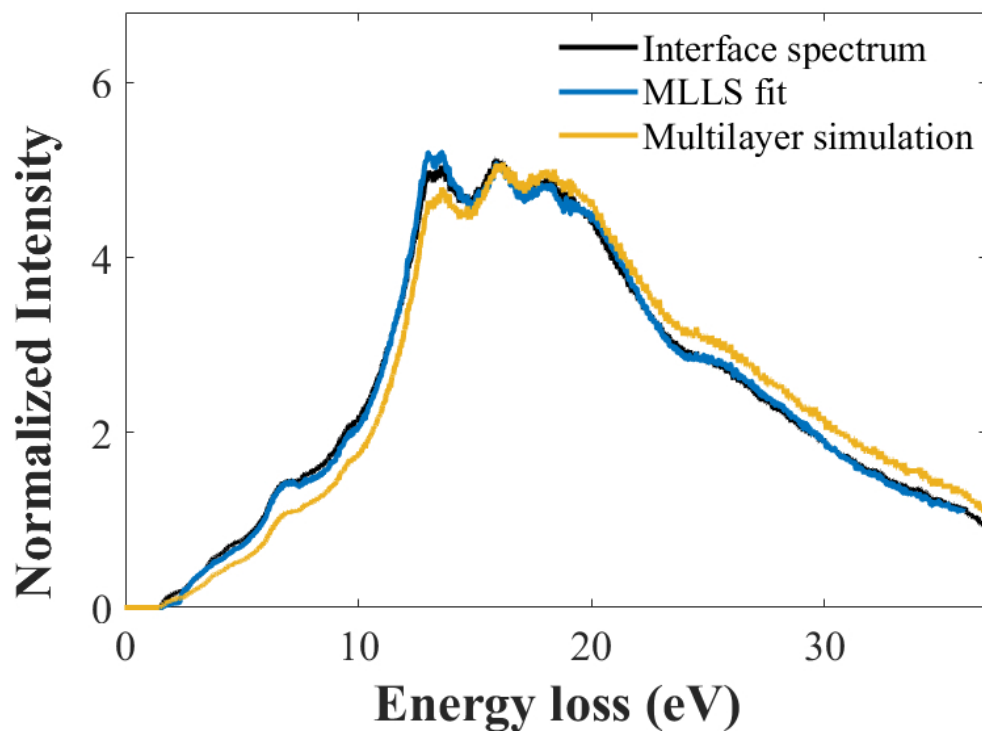


Fig1c

201x147mm (96 x 96 DPI)

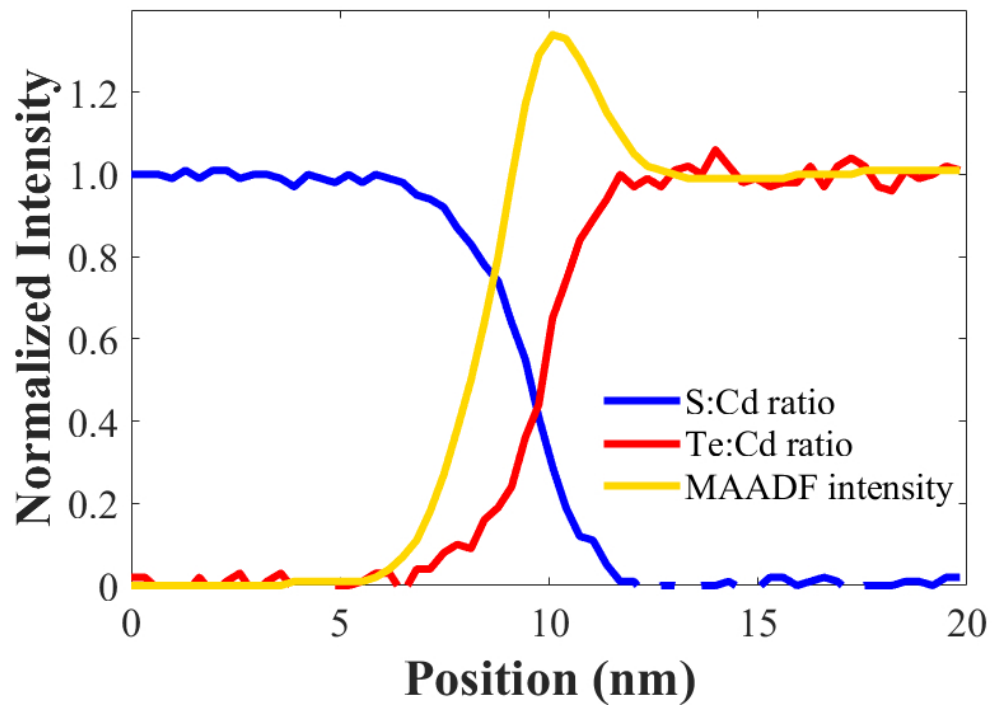


Fig1d

207x147mm (96 x 96 DPI)

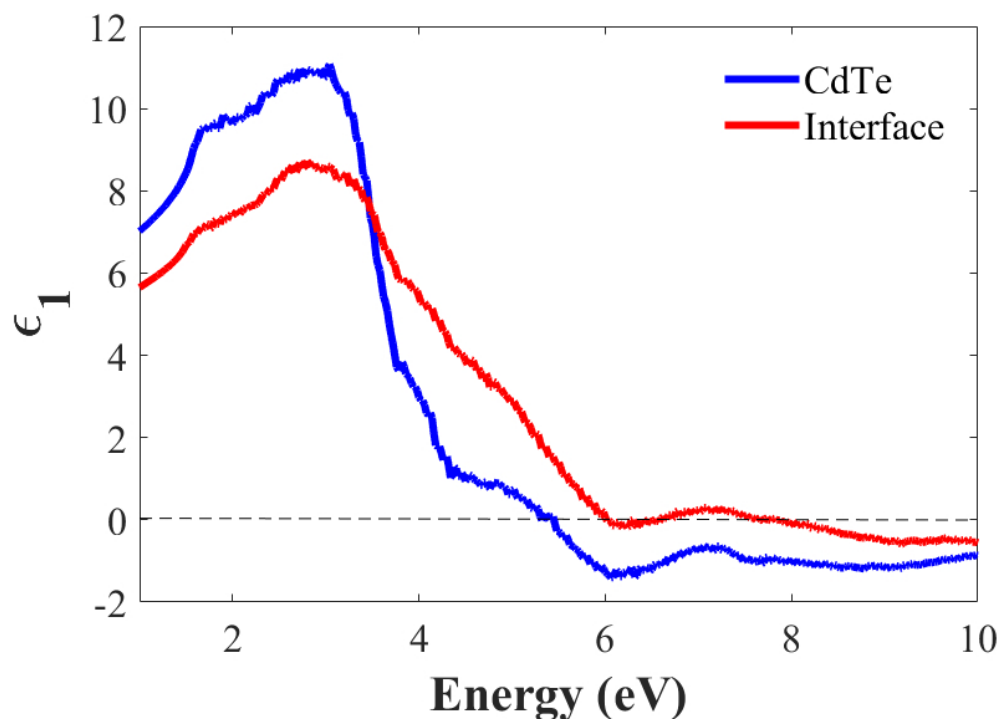


Figure 2a

212x154mm (96 x 96 DPI)

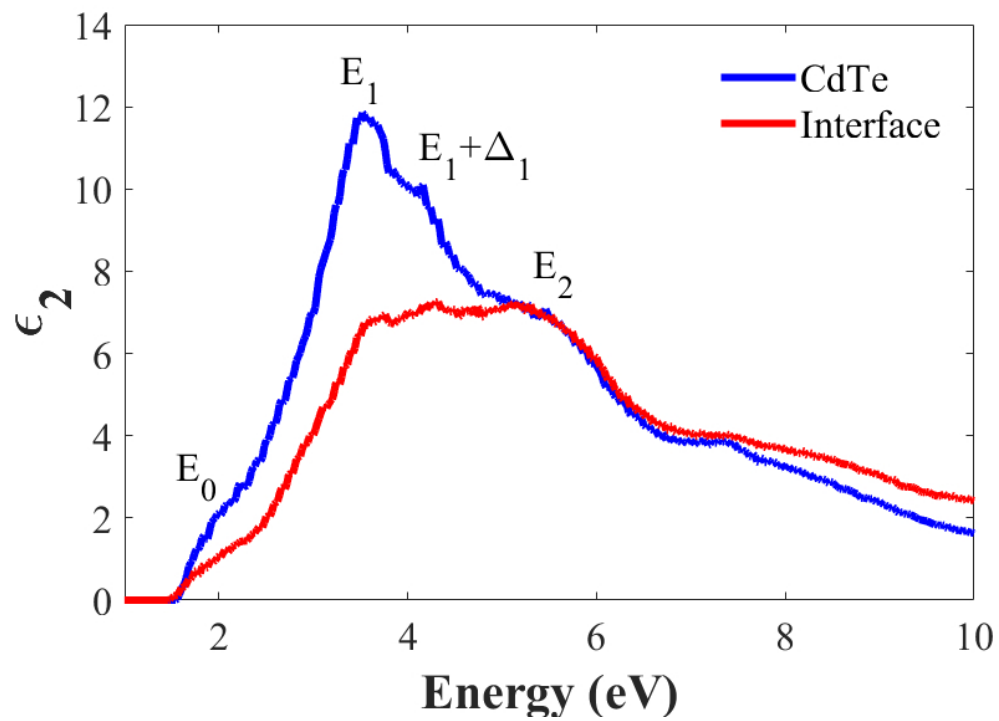


Figure 2b

212x153mm (96 x 96 DPI)

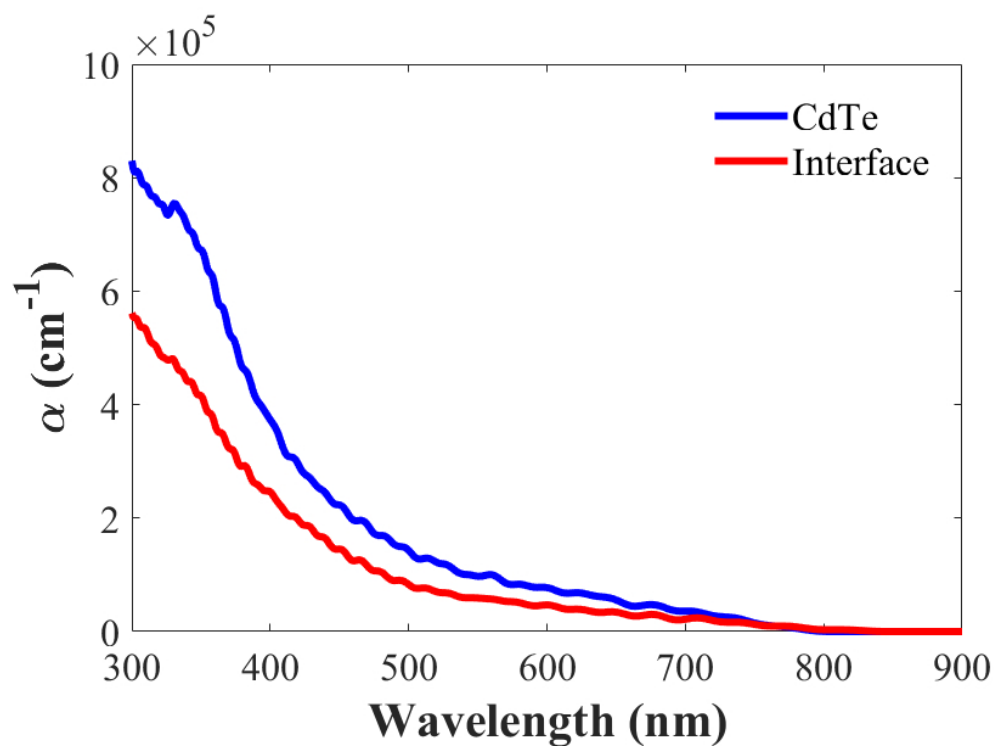


Figure 2c

217x160mm (96 x 96 DPI)

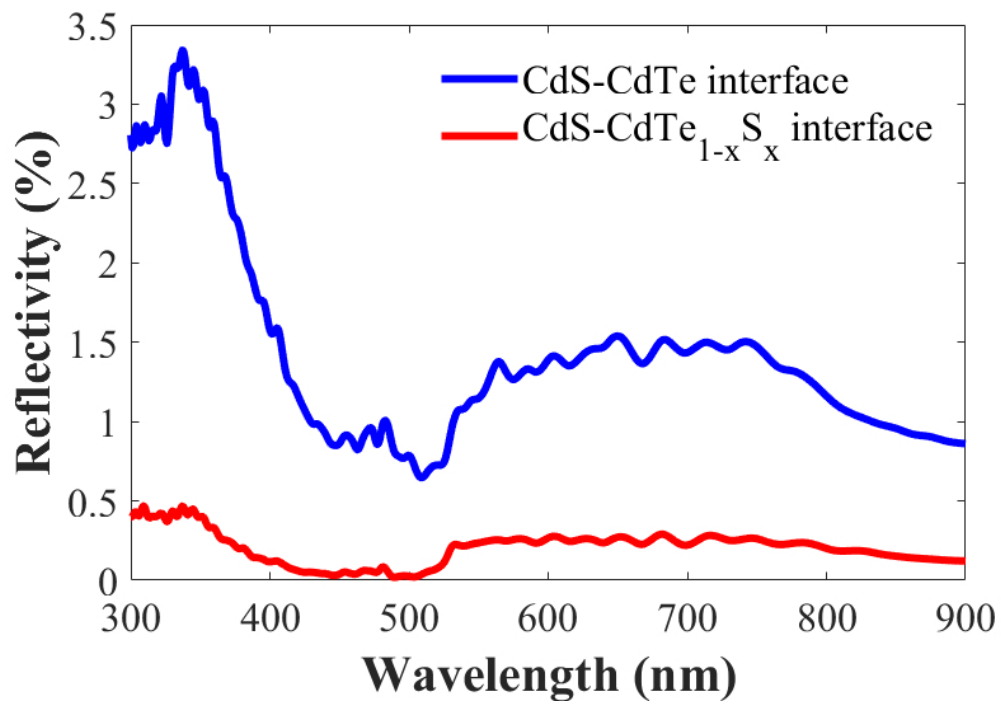


Figure 2d

208x148mm (96 x 96 DPI)

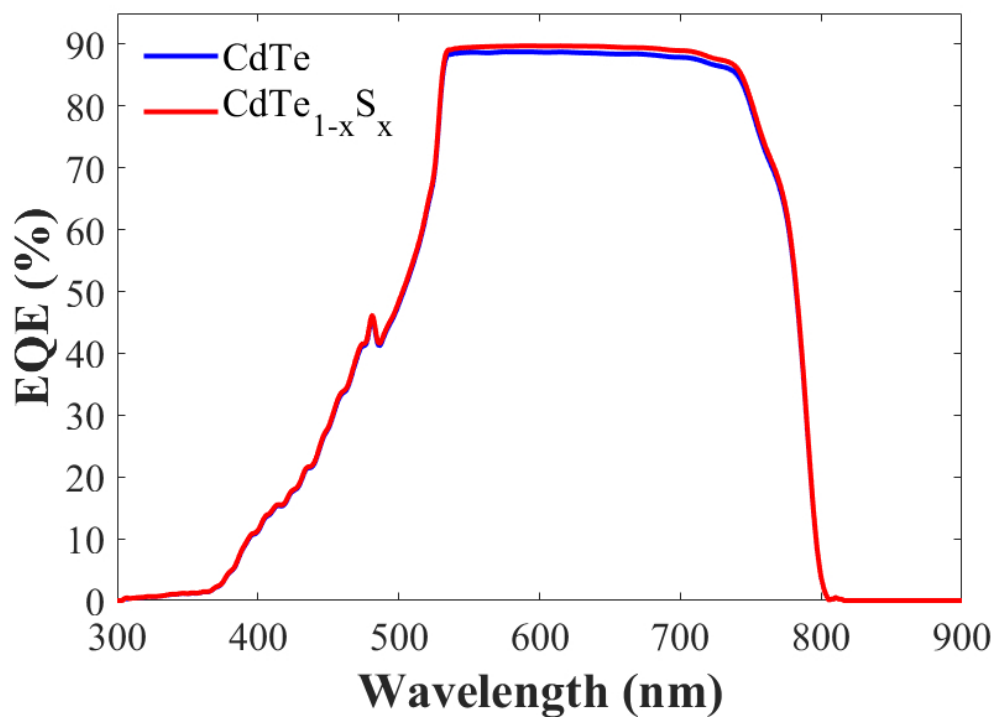


Figure 2e

213x153mm (96 x 96 DPI)

1
2
3
4
5
6
7
8
9
10
11
12
13
14
15
16
17
18
19
20
21
22
23
24
25
26
27
28
29
30
31
32
33
34
35
36
37
38
39
40
41
42
43
44
45
46
47
48
49
50
51
52
53
54
55
56
57
58
59
60

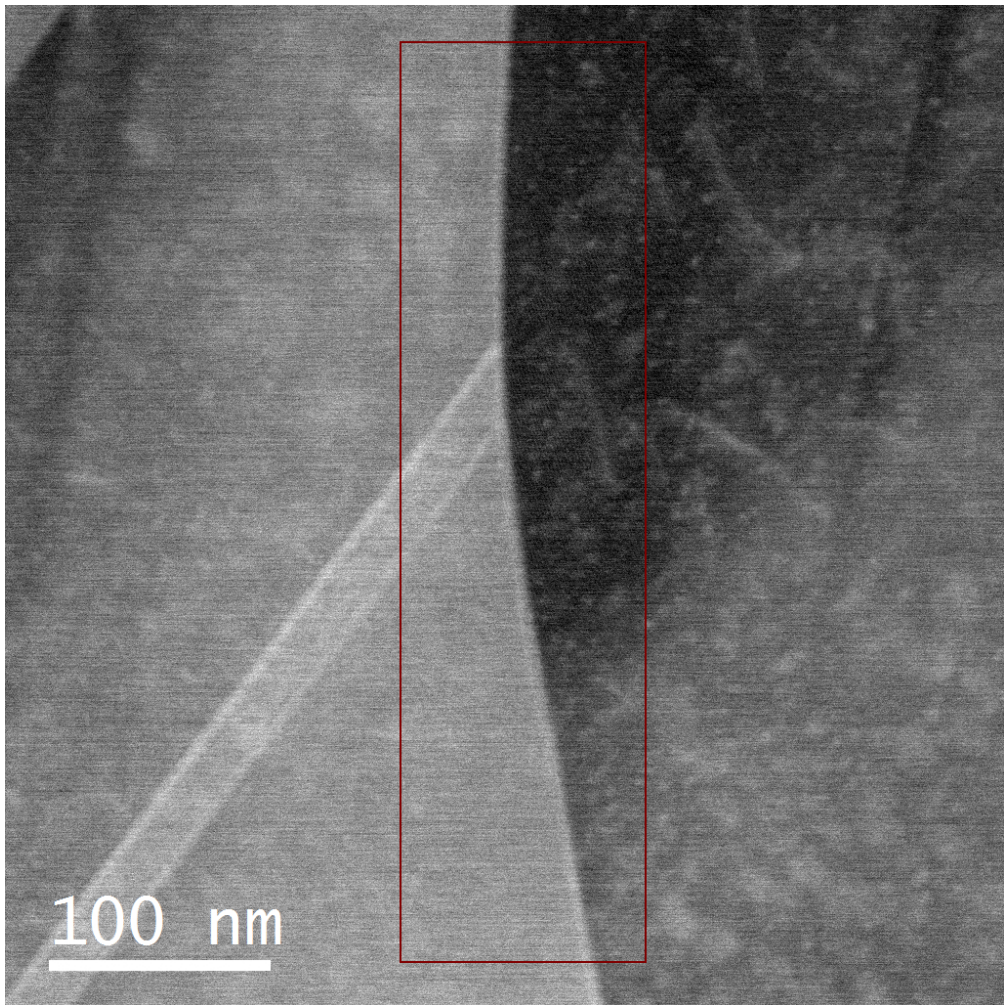


Figure 3a



Figure 3b

46x170mm (150 x 150 DPI)

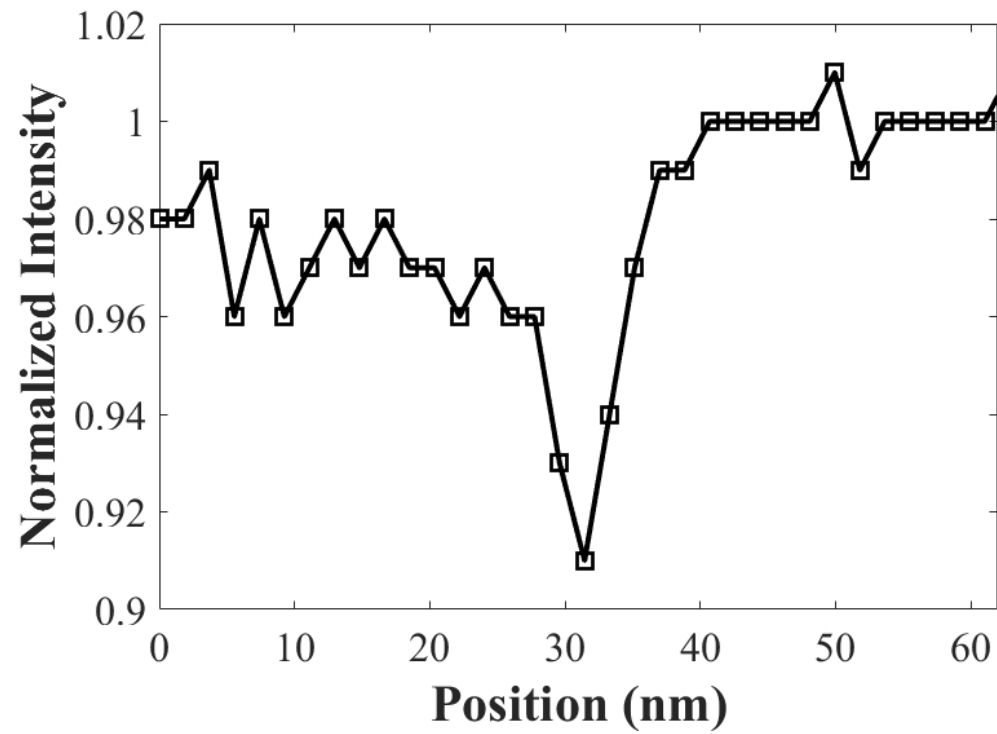


Fig3c

204x150mm (96 x 96 DPI)

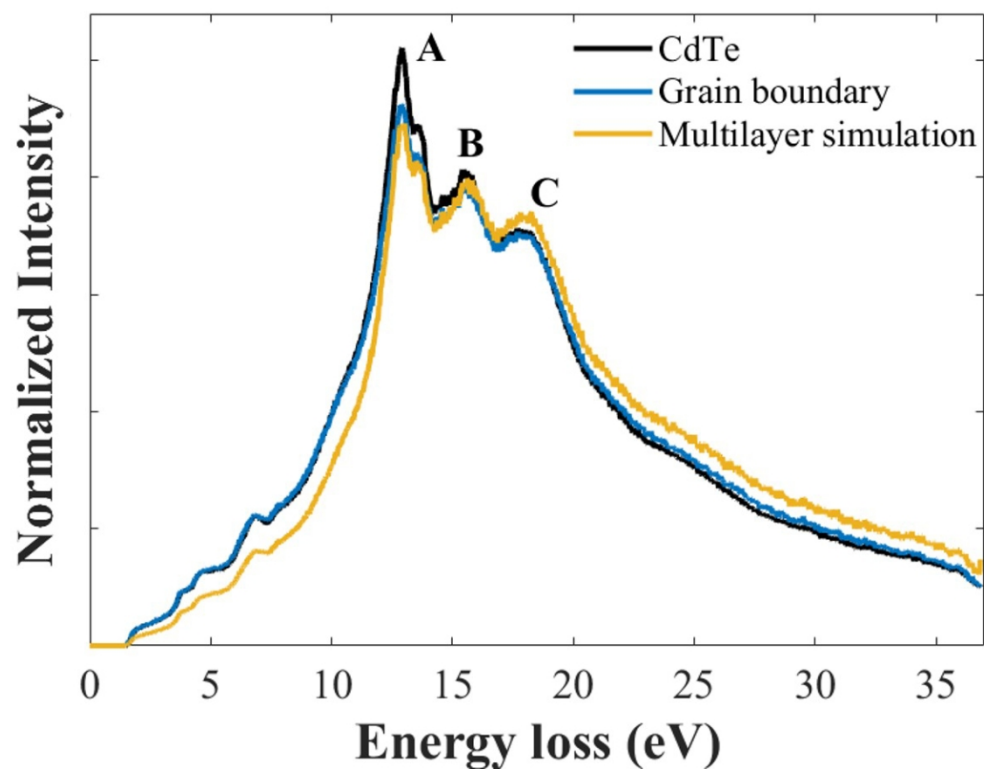


Fig4a

202x155mm (150 x 150 DPI)

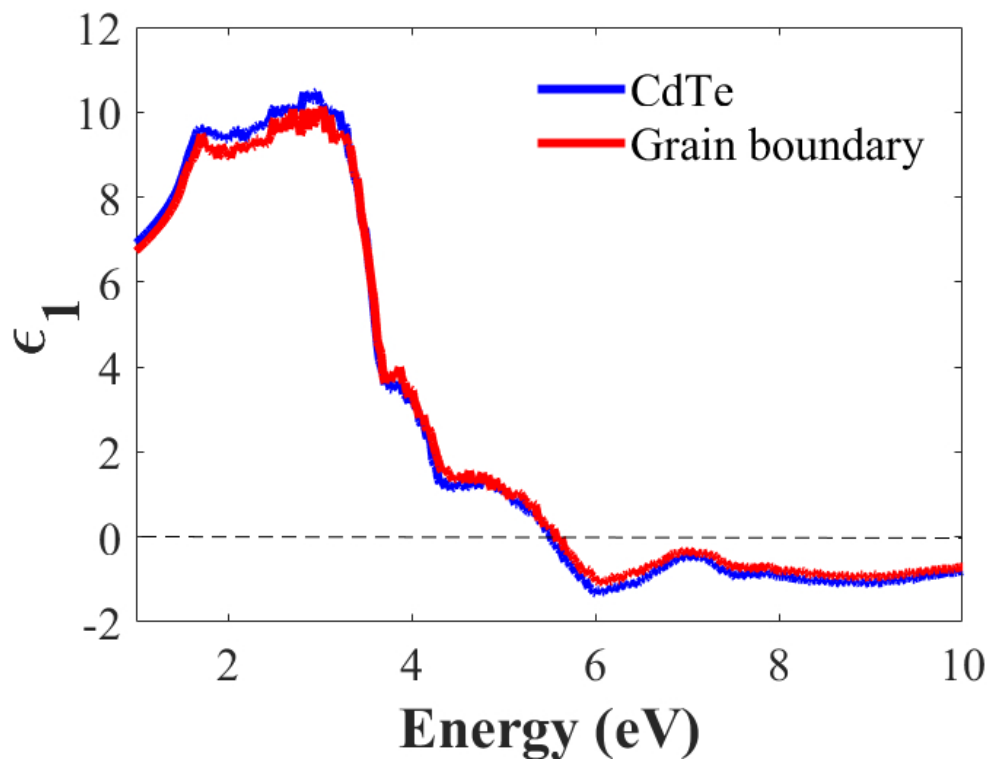


Figure 4b

181x138mm (96 x 96 DPI)

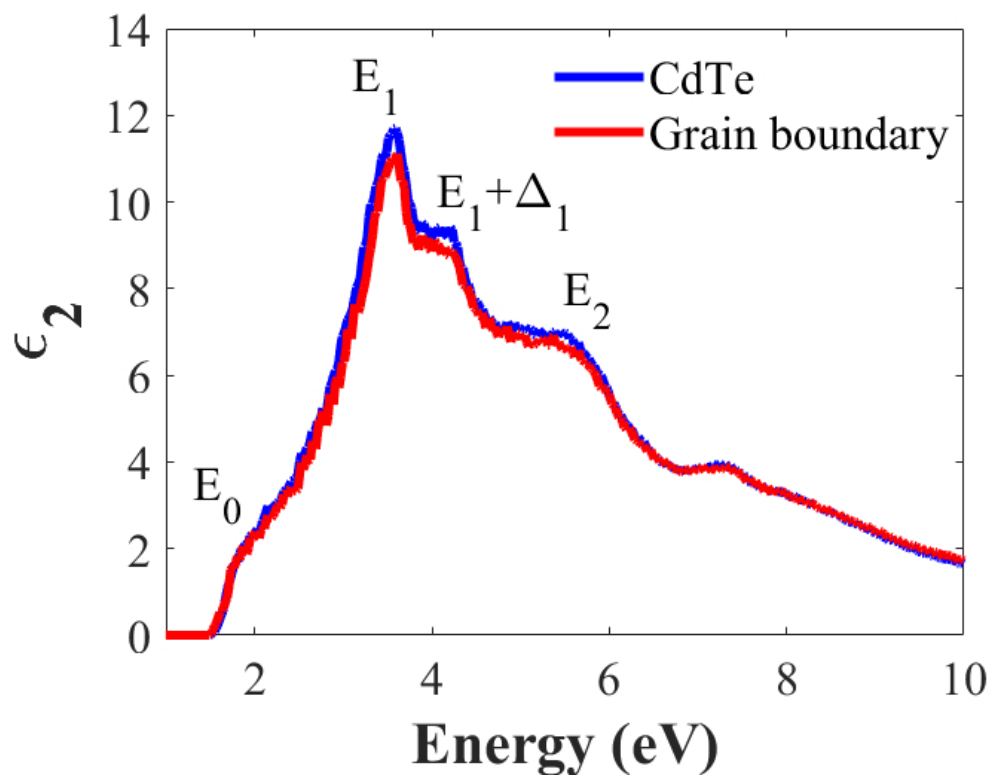


Figure 4c

178x138mm (96 x 96 DPI)

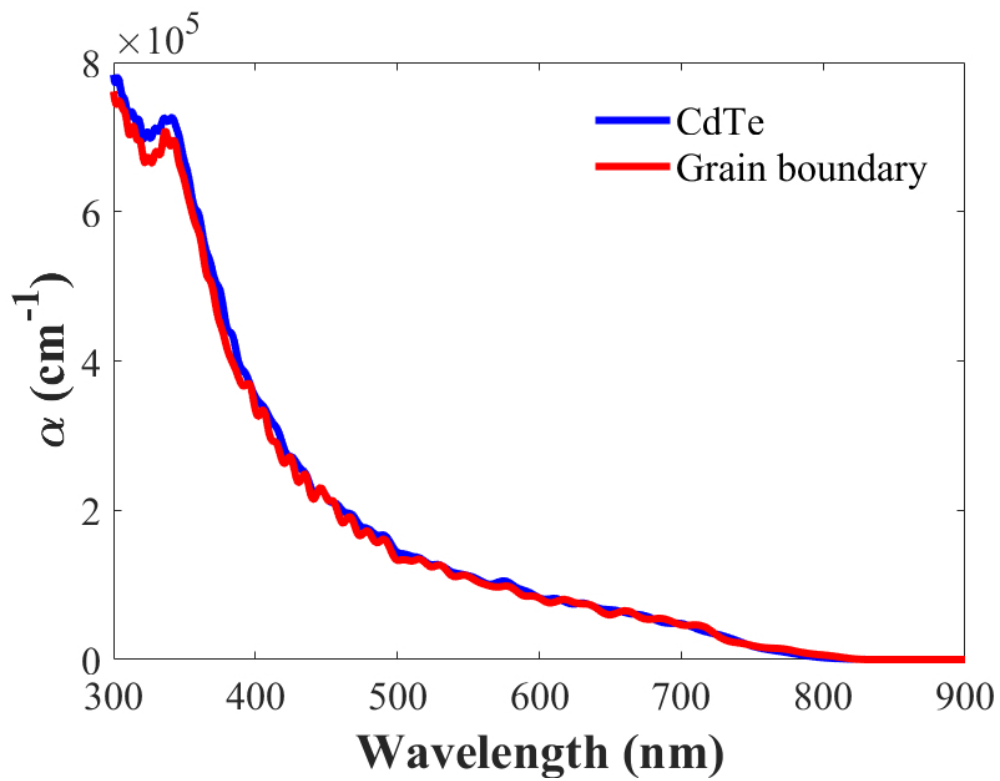


Figure 4d

212x164mm (96 x 96 DPI)

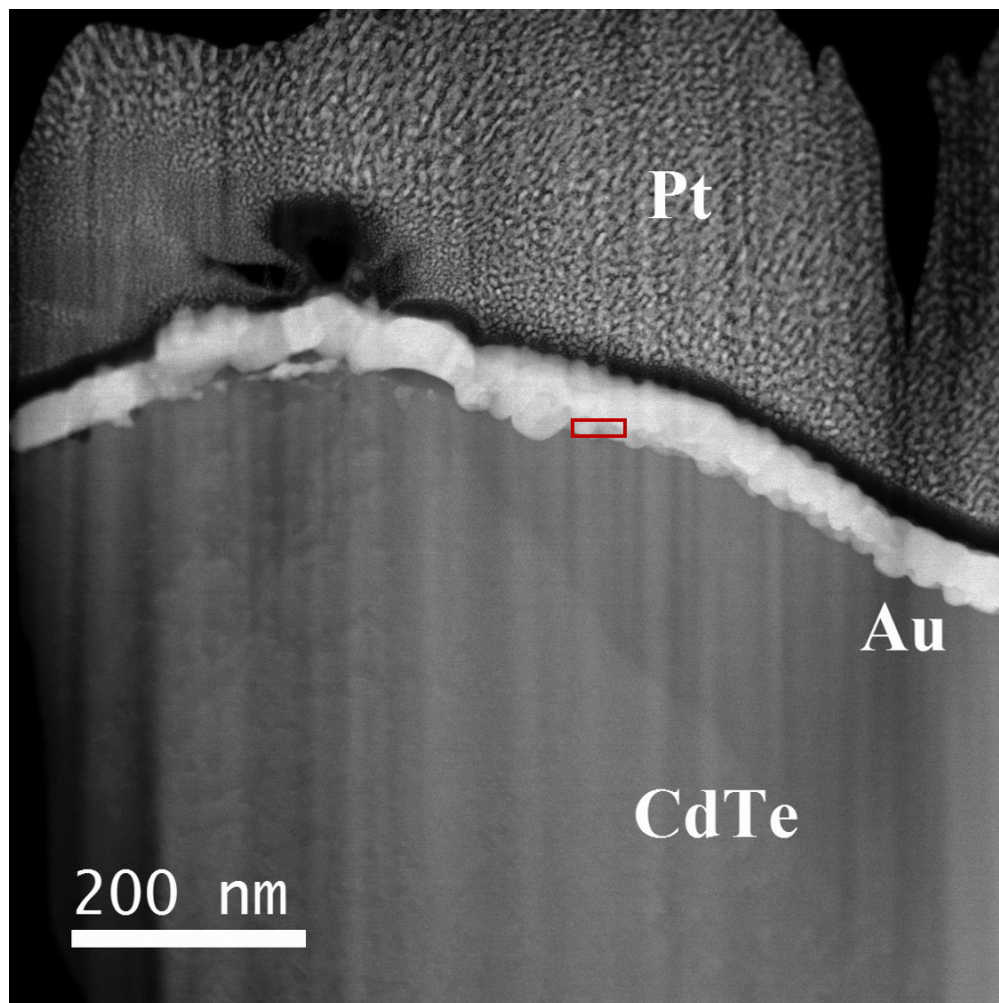


Figure 5a

190x190mm (150 x 150 DPI)

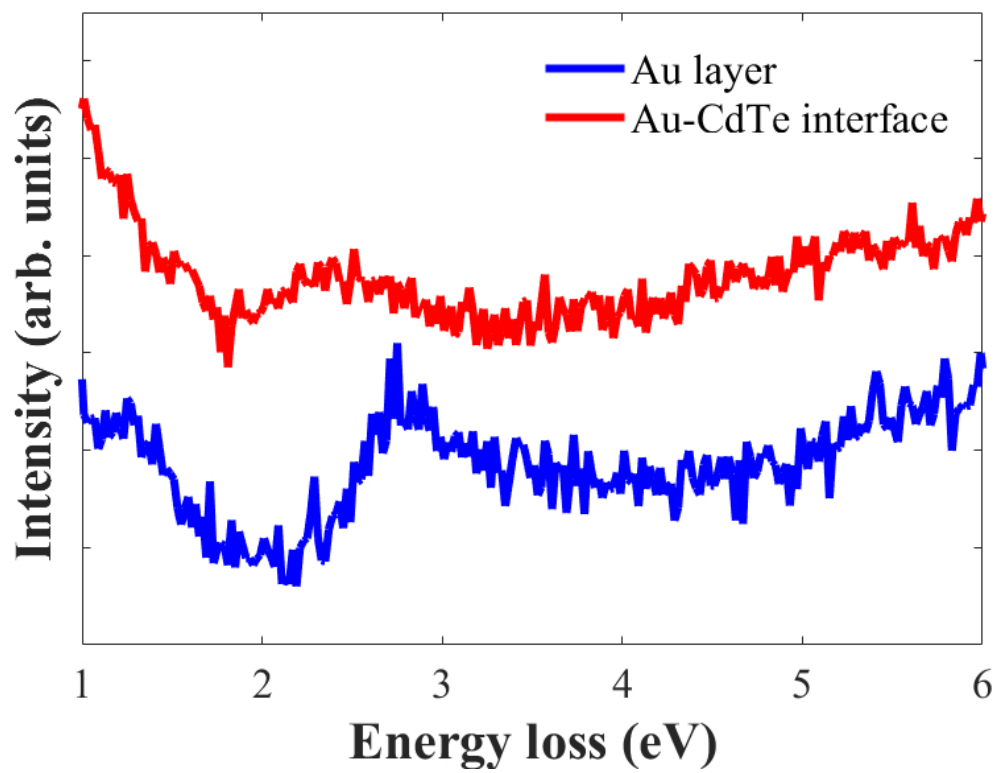


Figure 5b

200x156mm (96 x 96 DPI)

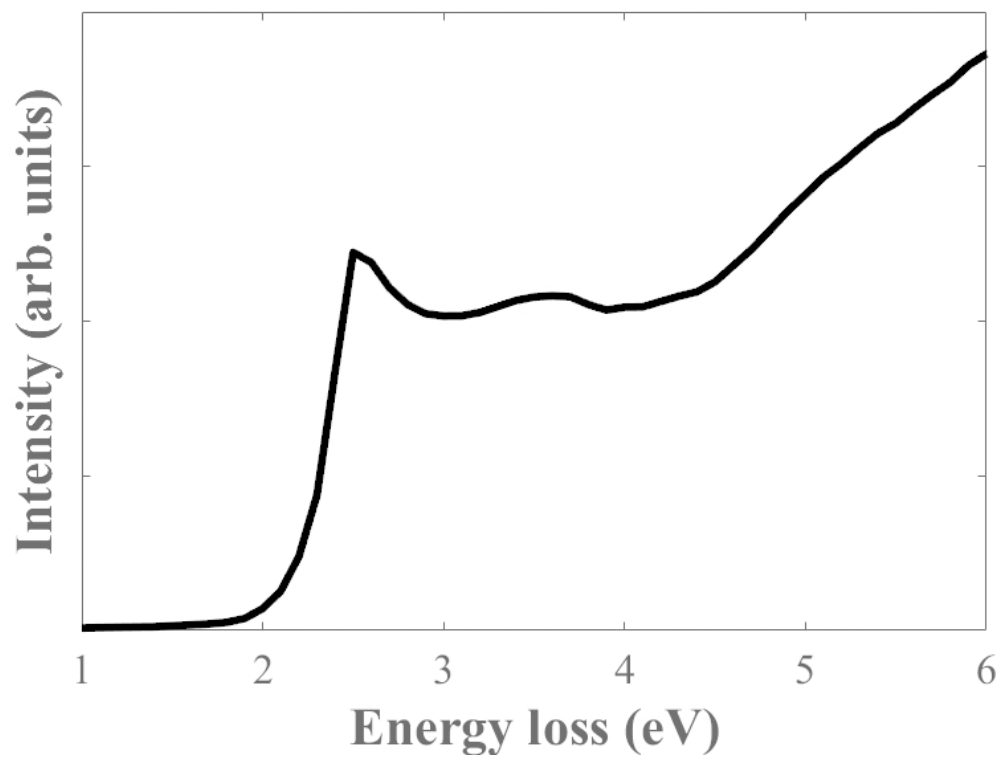


Figure 5c

199x151mm (96 x 96 DPI)

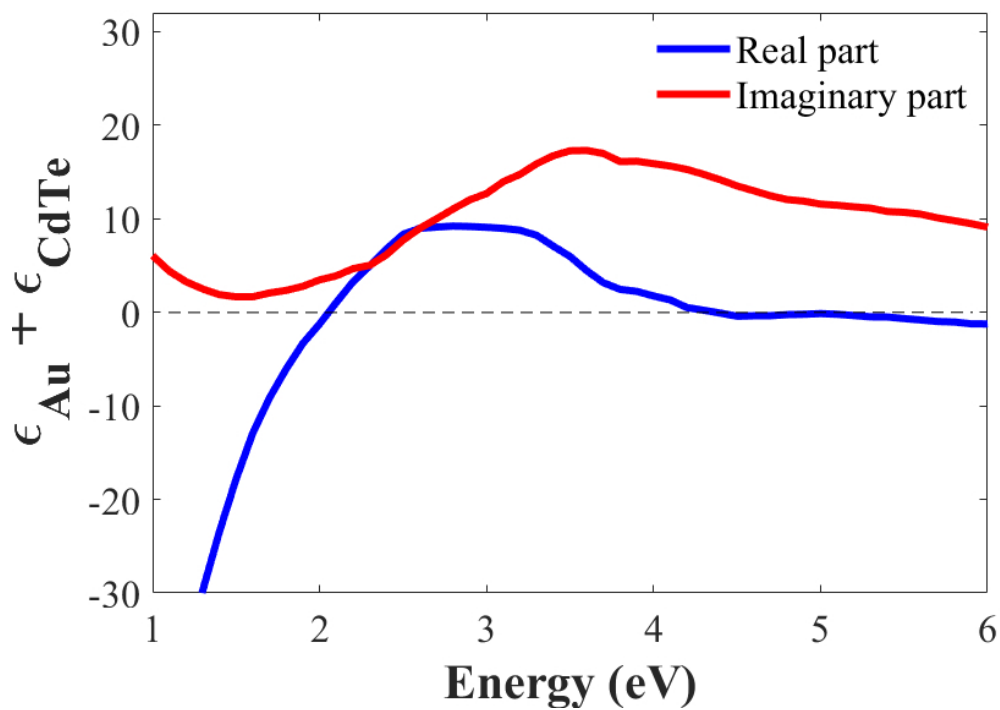


Figure 5d

216x157mm (96 x 96 DPI)

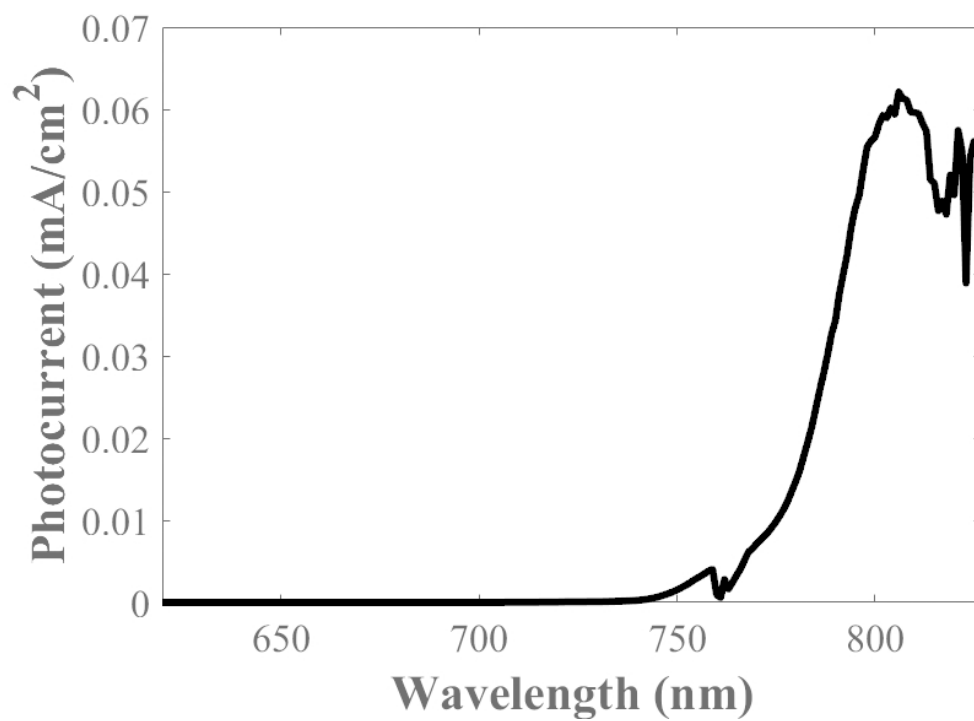
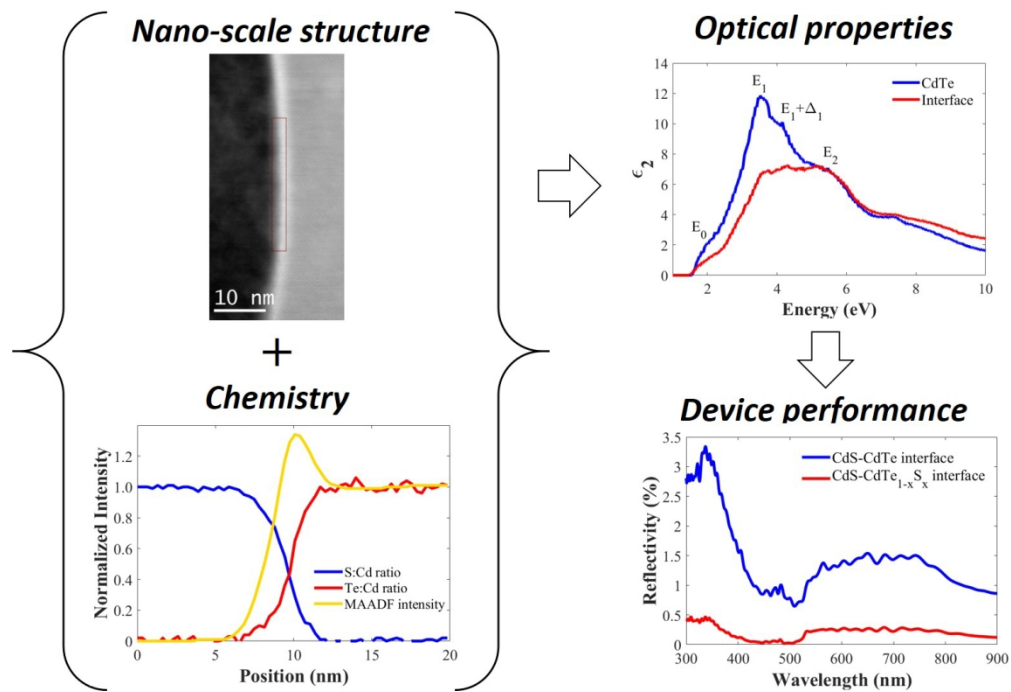


Figure 6

215x156mm (96 x 96 DPI)



Graphical abstract

263x183mm (150 x 150 DPI)